Application of a roughness-length representation to parameterize energy loss in 3-D numerical simulations of large rivers

S. D. Sandbach,[1,2] S. N. Lane,[3] R. J. Hardy,[1] M. L. Amsler,[4] P. J. Ashworth,[5] J. L. Best,[6] A. P. Nicholas,[2] O. Orfeo,[7] D. R. Parsons,[8] A. J. H. Reesink,[5,8,9] and R. N. Szupiany[4]

Received 15 August 2011; revised 23 October 2012; accepted 25 October 2012; published 6 December 2012.

[1] Recent technological advances in remote sensing have enabled investigation of the morphodynamics and hydrodynamics of large rivers. However, measuring topography and flow in these very large rivers is time consuming and thus often constrains the spatial resolution and reach-length scales that can be monitored. Similar constraints exist for computational fluid dynamics (CFD) studies of large rivers, requiring maximization of mesh- or grid-cell dimensions and implying a reduction in the representation of bedform-roughness elements that are of the order of a model grid cell or less, even if they are represented in available topographic data. These "subgrid" elements must be parameterized, and this paper applies and considers the impact of roughness-length treatments that include the effect of bed roughness due to "unmeasured" topography. CFD predictions were found to be sensitive to the roughness-length specification. Model optimization was based on acoustic Doppler current profiler measurements and estimates of the water surface slope for a variety of roughness lengths. This proved difficult as the metrics used to assess optimal model performance diverged due to the effects of large bedforms that are not well parameterized in roughness-length treatments. However, the general spatial flow patterns are effectively predicted by the model. Changes in roughness length were shown to have a major impact upon flow routing at the channel scale. The results also indicate an absence of secondary flow circulation cells in the reached studied, and suggest simpler two-dimensional models may have great utility in the investigation of flow within large rivers.

Citation: Sandbach, S. D. et al. (2012), Application of a roughness-length representation to parameterize energy loss in 3-D numerical simulations of large rivers, *Water Resour. Res.*, *48*, W12501, doi:10.1029/2011WR011284.

1. Introduction

[2] The world's largest rivers remain significantly understudied, despite the fact that they dominate the Earth's surface in terms of drainage and basin sedimentation, with almost half of the Earth's surface drained by its 50 largest rivers [*Potter*, 1978; *Ashworth and Lewin*, 2012]. Evidence also suggests that not all processes that influence river dynamics scale uniformly with increasing channel size. For example, *Parsons et al.* [2007] reported a marked lack of secondary flow structure in a large confluence-diffluence of the Río Paraná Argentina. Although *Parsons et al.* [2007] noted that dune morphology appeared to scale with flow depth, they observed that the channels had a high width-depth ratio and also there may be a much slower adjustment of dune morphology to changes in river discharge, both of which might dampen the formation of secondary circulations. Such observations emphasize the need for investigation of roughness effects in large rivers.

[3] A typical large river has lengths, widths, and depths of the order 10^3 km, 10^3 m, and 10^1 m, respectively, with discharge and sediment loads up to 200×10^9 m^3 and 1×10^9 t yr^{-1} [*Gupta*, 2007]. These large scales have been a prohibitive factor in field studies, constraining our ability

[1]Department of Geography, Durham University, Durham, UK.
[2]College of Life and Environmental Sciences, University of Exeter, Exeter, UK.
[3]Institut de Géographie, Faculté des Géosciences et de l'Environnement, Université de Lausanne, Bâtiment Anthropole, Lausanne, Switzerland.
[4]Universidad Nacional del Litoral, Facultad de Ingeniería y Ciencias Hídricas, Centro Internacional de Estudios de Grandes Ríos, Santa Fe, Argentina.
[5]Division of Geography and Geology, School of Environment and Technology, University of Brighton, Brighton, UK.
[6]Departments of Geology, Geography and Geographic Information Science and Mechanical Science and Engineering and Ven Te Chow Hydrosystems Laboratory, University of Illinois at Urbana-Champaign, Urbana, Illinois, USA.
[7]Centro de Ecologia Aplicada del Litoral, Consejo Nacional de Investigaciones Cientificas y Tecnicas, Corrientes, Argentina.
[8]Faculty of Science, Department of Geography, Environment and Earth Sceinces, University of Hull, Hull, UK.
[9]School of Geography, Earth and Environmental Sciences, University of Birmingham, Birmingham, UK.

Corresponding author: S. D. Sandbach, Department of Geography, Durham University, Durham DH1 3LE, UK. (s.sandbach@exeter.ac.uk)

0043-1397/12/2011WR011284

to investigate flow and morphology. However, technological innovations, notably in remote sensing of river-bed topography and measurement of river flow, have made quantitative investigations of large rivers increasingly feasible [e.g., *Richardson and Thorne*, 1998; *McLelland et al.*, 1999; *Ashworth et al.*, 2000; *Rennie et al.*, 2002; *Kostaschuk et al.*, 2004, 2005; *Parsons et al.*, 2005, 2007; *Rennie and Rainville*, 2006; *Viscardi et al.*, 2006; *Lane et al.*, 2008; *Szupiany et al.*, 2009].

[4] There is also a growing track record of effective application of hydrodynamic models to the quantification of river-channel hydrodynamics in both two dimensions (2-D) and three dimensions (3-D) [e.g., *Olsen and Stokseth*, 1995; *Hodskinson*, 1996; *Ferguson et al.*, 2003; *Lane et al.*, 1999, 2000, 2004; *Ma et al.*, 2002; *Booker et al.*, 2001, 2004; *Rodriguez et al.*, 2004; *Nicholas*, 2001, 2005; *Ruther et al.*, 2005; *Ruther and Olsen*, 2007; *Tritthart and Gutnecht*, 2007; *Abad et al.*, 2008; *Shen and Diplas*, 2008; *Tritthart et al.*, 2009], and some of these studies have begun to consider large rivers [e.g., *Kleinhans et al.*, 2008; *Ercan and Younis*, 2009]. A critical element of such application is the representation of bed roughness elements, which range from individual grains of sand up to large bedforms such as dunes. Modeling these elements is explicitly possible at very high resolutions [e.g., *Lane et al.*, 2004; *Hardy et al.*, 2006], but for river-scale applications, resolving even dune-size bedforms can be difficult due to the computational resources required as well as the availability of topographic data that are constantly evolving. Recent advances in numerical modeling techniques have been aimed at improving this situation. For example, *Nabi* [2008a, 2008b] used an unstructured grid that could be refined in all dimensions, in particular close to the bed, and successfully coupled a discrete particle model to a large eddy simulation. This technique may provide an alternative method for specifying bed topography. However, it still does not address the computational demands associated with running models with resolutions of a meter or less (to resolve dunes, for example) over spatial scales of several kilometers. It also does not address the fact that large-scale bathymetric surveys are required that may only be applicable to a small range of flow conditions. For this reason, parameterization of bed roughness remains necessary.

[5] In both one-dimensional (1-D) and 2-D simulations of river flows, velocity predictions have proven to be highly sensitive to roughness parameterization [*Lane and Richards*, 1998; *Lane*, 2005], and this has made it a primary modeling consideration. Much of this work has focused upon developing robust mathematical descriptions to capture the interactions between near-bed flow velocity, grain, and bedform descriptors of the river-bed surface and fluid turbulence [e.g., *Clifford et al.*, 1992; *Ferguson*, 2007]. However, in practice, bed roughness tends to be used as a calibration parameter so as to force agreement between model predictions and field observations [*Lane*, 2005].

[6] The majority of hydrodynamic models of river flow parameterize roughness effects through the application of a logarithmic friction law [e.g., *Hodskinson*, 1996; *Hodskinson and Ferguson*, 1998; *Lane et al.*, 1999, 2000, 2004; *Booker et al.*, 2001; *Morvan et al.*, 2002; *Booker*, 2003; *Olsen*, 2003; *Booker et al.*, 2004; *Dargahi*, 2004; *Rodriguez et al.*, 2004; *Ruther et al.*, 2005; *Ruther and Olsen*, 2007; *Tritthart and Gutnecht*, 2007; *Abad et al.*, 2008; *Kleinhans et al.*, 2008; *Shen and Diplas*, 2008; *Ercan and Younis*, 2009; *Tritthart et al.*, 2009]. In this formulation, the roughness parameter k_s, often referred to as Nikuradse sand roughness [*Nikuradse*, 1933], is used to characterize the effect that roughness elements have on the flow. The value of k_s is normally set as a function of a measured grain-size diameter [e.g., *Abad et al.*, 2008; *Shen and Diplas*, 2008]. The development of more sophisticated roughness parameterizations to deal with other types of energy losses, such as those associated with secondary circulation [e.g., *Blanckaert and de Vriend*, 2003, 2010] and curvature-driven turbulence [e.g., *Blanckaert*, 2009], have also been investigated.

[7] In many of the above examples, roughness is being used as an effective parameter in an auxiliary relationship that is required to represent energy losses that are not otherwise being represented explicitly. The simplest approach to this problem is to identify a generic auxiliary relation (i.e., one that applies throughout the computational domain) and then to consider how to represent the roughness parameter. This has involved both friction factor-based [e.g., *Dargahi*, 2004] or an analytical [e.g., *van Rijn*, 1984, 2007; *Olsen*, 2003; *Ruther et al.*, 2005; *Ruther and Olsen*, 2007; *Paarlberg et al.*, 2010] upscaling to the sand roughness. Some applications have explored the sensitivity of model predictions to roughness parameterization [e.g., *Kleinhans et al.*, 2008; *van Balen et al.*, 2010]. Less common approaches include inference of the sand roughness from estimates of Manning's n [*Morvan et al.*, 2002] and the use of roughness lengths measured directly from velocity profiles [*Hodskinson*, 1996]. A small number of studies (including the present paper) have sought to optimize model predictions (e.g., water-surface elevation; velocity) on experimental or field measurements by adjusting the roughness length [e.g., *Booker*, 2003; *Rodriguez et al.*, 2004; *Tritthart and Gutnecht*, 2007; *Tritthart et al.*, 2009]. The majority of these approaches apply estimates of sand roughness that are derived from reach to bar-form scales, and thus are more suited to 1-D and 2-D approaches. For example, the *van Rijn* [1984, 2007] roughness predictors are based on depth-averaged values of flow, whereas friction factor- and Manning's n-based estimates provide a reach-averaged approximation.

[8] Other studies have shown the merits of moving away from the log-law formulation altogether through new types of auxiliary relations. Both *Nicholas* [2005] and *Carney et al.* [2006] developed formulations more sensitive to the presence of bedforms, whereas *Kang and Sotiropoulos* [2011] solved the boundary layer equation, and *Constantinescu et al.* [2011] employed a detached eddy simulation (DES) that is capable of resolving near-wall flow with more accuracy than wall functions. A very fine mesh is employed with only grain roughness parameterized, and so application here would not be possible, given computational restraints especially at these large scales. *Escauriaza and Sotiropoulos* [2011] also applied DES coupled with a sediment transport model, using a numerical scheme that contains predetermined dissipation to include the effect of subgrid topography that is scale dependent and requires parameterization [*Escauriaza and Sotiropoulos*, 2011]. The double-averaging approach [*Nikora et al.*, 2007a, 2007b] appears to offer a way forward in this respect. The resulting set of equations, known as the double-averaged Navier Stokes (DANS) equations,

include an additional stress term that is referred to as the form-induced stress. This is analogous to the Reynolds stress but results from spatial rather than temporal variations in mean velocity. Near the bed, this stress can be a similar order of magnitude to the Reynolds stress [*Nikora et al.*, 2007b]. Adopting such an approach to estimate roughness, a priori, in a mathematical model, requires very high-resolution field data to calculate the DANS terms, and such data may not be available in large river studies, although this is the approach that is likely to be most robust in this kind of study.

[9] In summary, the application of a 3-D model that captures bedform roughness effects is possible. At very large scales, this becomes increasing difficult, and thus parameterization of bedform roughness elements may be required. However, there is no clear established theory for defining what the effective roughness length should be in a 3-D simulation. This length should vary with both unmeasured elements of bed topography and be dependent on the data-collection spacing (e.g., dune morphology) and the resolution of numerical discretization. This variation should also be both temporal [*van Rijn*, 1984, 2007] and spatial [*Nicholas*, 2005; *Zeng et al.*, 2008; *van Balen et al.*, 2010], but, in a deterministic sense and with the resolution of topographic data that can be achieved over large extents in wide rivers, such a deterministic approach is not possible. Additionally, the sensitivity of models to a spatial variability in roughness specification has been tested and revealed relatively small differences in the global flow distribution [*Viscardi et al.*, 2006; *van Balen et al.*, 2010], although some differences in secondary flow characteristics and bed shear stress distributions were observed [*van Balen et al.*, 2010]. Moreover, there are few comparisons of different wall treatments and a limited number of studies that have fully tested the sensitivity of model predictions to model parameterization, although *Ercan and Younis* [2009] and *Kleinhans et al.* [2008] are notable exceptions. *Kleinhans et al.* [2008] studied the dynamics of channel bifurcations and tested a 3-D model for sensitivity to a number of factors, including the type of roughness specification. *Kleinhans et al.* [2008] employed both uniform Chezy and Colebrook-White formulations, and their results did not indicate a preference for either parameterization. *Ercan and Younis* [2009] investigated the uncertainty in model predictions of flow along a reach of the Sacramento River and tested the sensitivity of the model predictions to various modeling parameters, such as grid resolution, turbulence closure, and roughness parameterization. To assess the sensitivity of model predictions to the type of roughness formulation, they compared their predictions with measured data, and the model predictions were obtained using their 2-D model with Colebrook-White, Manning, and Blasius formulations to specify roughness. The Colebrook-White and Manning formulations were found to give similar results and compared more favorably to measured data than the Blasius formulation.

[10] The aim of the present paper is to explore the impacts of roughness length upon key characteristics of the 3-D flow field in large rivers and to consider its implications for parameterization of roughness effects in both 3-D and 2-D depth-averaged model formulations. The purpose of this study is as follows: (1) to assess roughness length parameterization in the application of computational fluid dynamics (CFD) of large rivers, (2) to test the sensitivity of the model to roughness length specification, (3) to assess the implications of roughness treatments that assume the velocity profile is log-linear and 3-D simulations that use the fully rough log-law, and (4) to investigate the flow field using CFD output. This is achieved through the application of a CFD model informed by field measurements of flow and bed topography. The model is run with a roughness-length parameterization, and a range of roughness-length values are implemented, allowing investigation of this influence on flow routing and validation with measured flow data. These results are analyzed in four parts: (1) modeled and measured data are directly compared and a number of metrics are used to assess the optimal roughness length; quantitative assessment of the spatial velocity fields is also given; (2) the sensitivity of flow routing is investigated; (3) assessment of a number of velocity profiles extracted from the CFD predictions distributed spatially through the reach is presented; these results are used to quantify the convergence between 3-D models that use the fully rough log-law and those that assume the flow to be logarithmic over the entire depth, and (4) primary and secondary flow patterns around, and in, the lee of a large bar are presented using the optimal CFD results. The paper commences by detailing the methods used to obtain the field data and the CFD model applied. This is followed by a presentation and discussion of the results obtained in section 3 followed by the conclusions in section 4.

2. Methodology

2.1. Study Area

[11] In the present paper, results from a coupled field and numerical-modeling study are presented. The field research was conducted along a 38 km reach in the middle part of the Río Paraná, Argentina (Figures 1a and 1b), one of the largest rivers in the world, with a drainage basin area of $\sim 2.6 \times 10$ km^2 [*Gupta*, 2007]. The study reach stretched from Itati to Paso de la Patria, which lies upstream of the confluence between the Río Paraná and the Río Paraguay (Figure 1c). In the study area, the mean annual discharge is $\sim$12,000 m^3 s^{-1} (measured at the Itati gauging station), the maximum bankfull discharge is $\sim$19,000 m^3 s^{-1}, and the water-surface slope is 4.4 cm km^{-1} [*Orfeo and Stevaux*, 2002]. Bed material in the study area is well sorted, predominantly medium-to-fine sand (average D_{50} of 26 bed samples is 0.35 mm), although some fine gravel is present in the channel thalweg and on eolian deflation surfaces on some exposed bars.

[12] The main bedforms in the Paraná are dunes, and these are evident at all flow stages [*Parsons et al.*, 2005; *Kostaschuk et al.*, 2009; *Shugar et al.*, 2010]. Multibeam measurements collected around a large bar ($\sim$3.5 km in length), just in front of the Río Paraná-Paraguay confluence, reveal mean dune heights and lengths of 1.5 and 64 m, respectively [*Parsons et al.*, 2005; *Sambrook Smith et al.*, 2009].

[13] Superimposed dunes with heights and lengths up to 0.3 and 10 m, respectively, were also measured when the discharge was estimated as 15,100 m^3 s^{-1} (cross section CS-A; Figure 1d). However, during a very large flood event ($Q \sim$ 36,000 m^3 s^{-1} in 1983), dune heights and

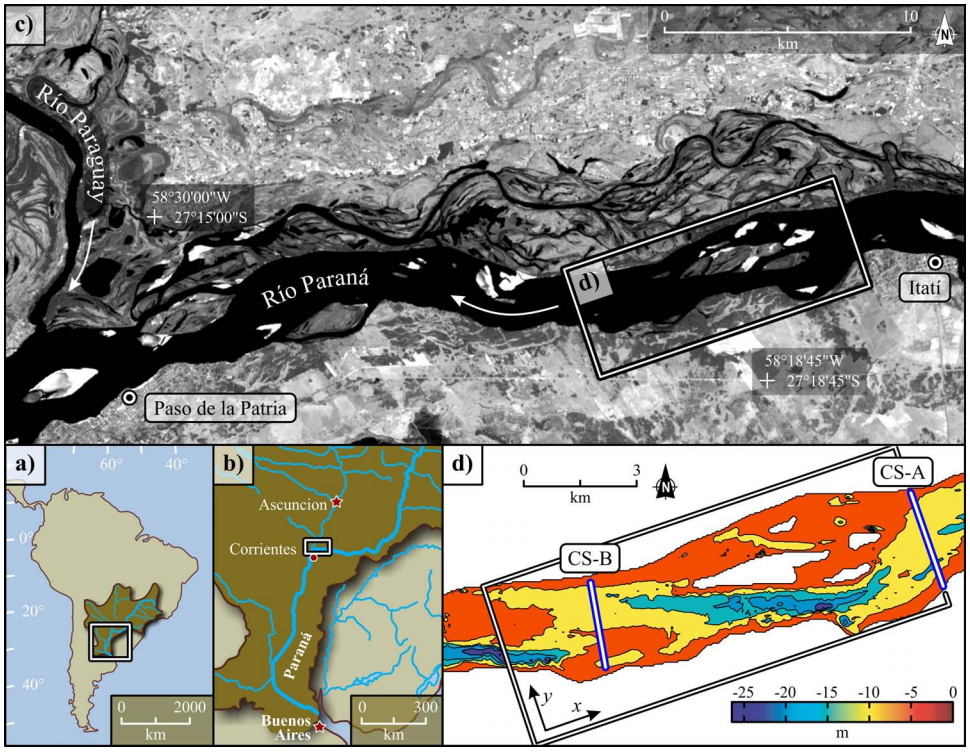

Figure 1. (a) Location of the study site in Argentina, South America. The reach is located close to (b) Corrientes City just upstream of the (c) Río Paraná-Paraguay confluence. Velocity and topographic data were collected during the field survey, and (c and d) the area modeled in this paper is highlighted. In (d), the locations of the ADCP data are depicted (A: inlet and B: validation). Satellite imagery (c) provided courtesy of the United States Geological Survey.

wavelengths of up to 6.5 and 320 m, respectively, have been observed within the Río Paraná [*Amsler and Garcia*, 1997]. Ripples are present in shallow water and are common on near-emergent bar tops [*Sambrook Smith et al.*, 2009].

2.2. Field Data Collection

[14] A combined bed topography and 3-D flow survey was conducted in the 38 km reach from two small research vessels during April 2008 [see *Sandbach et al.*, 2010]. In the present paper, an 11 km long region of this 38 km reach is modeled (indicated by the box shown in Figure 1c). This region was selected as it contained two acoustic Doppler current profiler (ADCP) transects (see Figure 1d): one used as a boundary condition (cross section CS-A) and the other for model validation (cross section CS-B). The digital elevation model (DEM) and the locations of the flow measurements are presented in Figure 1d. The flow measurements were collected between 18 and 20 April, during which time the flow discharge was ~15,100 $m^3\ s^{-1}$. Topographic data were collected between 13 and 18 April, and these measurements indicate that the mean depths and widths within the reach were 5.7 m and 2.8 km, respectively. The greatest depths were measured in thalweg scours up to 26 m deep, with a mean cross-sectional depth-averaged flow velocity around 1 $m\ s^{-1}$. These measurements indicate flow Reynolds numbers within the reach are of the order 5×10^6 and Froude numbers are approximately 0.1.

[15] Topographic data were obtained using a RESON Navisound 215 dual-frequency (33 and 210 kHz) single-beam echo sounder, collecting data at ~1 Hz, linked to a global positioning system (GPS). Topographic information was collected at a total of 163 cross sections, separated by approximately 200 m in the downstream direction and a series of longitudinal lines along the length of the reach. The survey did not pick out even the largest bedforms sufficiently to represent them explicitly in the model, and thus form roughness is specified using a roughness length treatment (detailed in the following section). The surveyed lines were projected onto a universal time meridian (UTM) coordinate system and postprocessed in Computer Aided Resource Information System (CARIS) Hydrographic Information Processing System (HIPS) software. Variations in water surface elevation during the topographic data collection period were corrected using stage-gauge data from within the reach. To produce the final DEM of the study reach, the topographic data were interpolated onto a regular grid of 50 m × 50 m using a kriging algorithm.

[16] The flow data was obtained using a Teledyne RDI 1200 kHz ADCP (Teledyne RD Instruments), which was set to determine 3-D flow in a vertical column at 0.5 m interval bins at a rate of ~1 Hz. The ADCP was deployed in moving-boat mode with vessel position and velocity correction provided via Real Time Kinetics (RTK) GPS. The locations of the ADCP cross sections are depicted in Figure 1d and Figure 2, labeled CS-A and CS-B. Following *Szupiany et al.* [2007], six repeat transects were collected at each cross

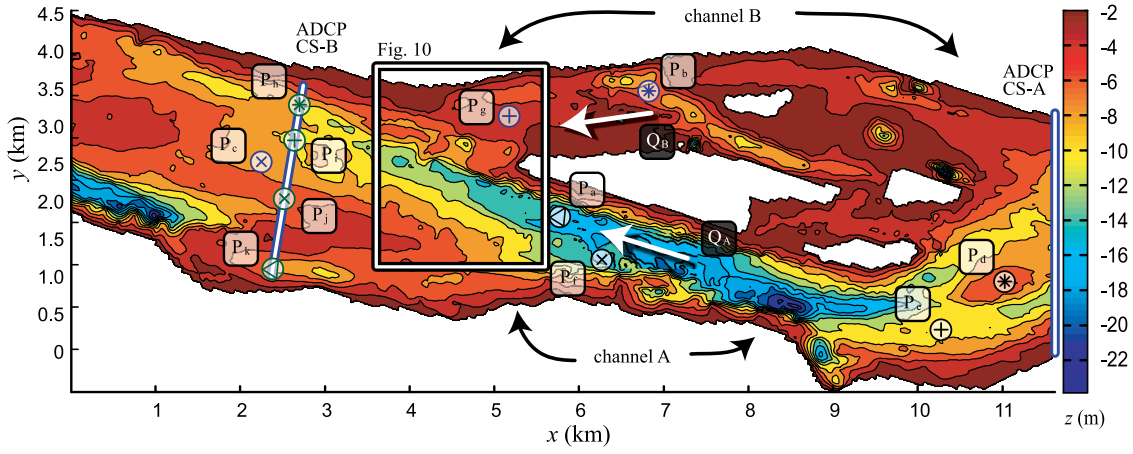

Figure 2. Detailed DEM of the area modeled with key locations and profiles P_a-P_k labeled. These are locations in the reach where we extract CFD data for further analysis. The box indicates the location of the postconfluence flow shown in Figure 10 and the location of the validation ADCP cross section (B in Figure 1d).

section to obtain a statistically stationary flow field. Average boat velocity during the ADCP surveys was 1.12 m s^{-1}, providing high-resolution (~4 measurements m^{-2}) velocity data along each cross section.

[17] The measurement error associated with moving-boat ensemble averaging is estimated to be 0.04 m s^{-1}. This estimate is based on a combination of ADCP error velocity, computed from the four-beam variation [see *Oberg and Mueller*, 2007], and a study of both a fixed vessel (time-averaged) and a moving vessel (ensemble-averaging) methodology previously conducted within the Río Paraná [*Szupiany et al.*, 2007]. The distance from the water surface to the first ADCP measurement bin was 0.74 m, which accounted for submergence of the ADCP below the waterline and the blanking distance that removes the effect of acoustic side-lobe ringing. Data from the bottom 6% of the profile were also removed in processing, again to remove the effect of contamination by side-lobe interference. This does not directly impact upon the modeling results, although it does affect the vertical extent of the domain that can be validated. Colocation of the flow and topographic data was achieved using the RTK GPS data.

2.3. Roughness-Length Representation

[18] *Garcia* [2006] has reviewed methods that account for subgrid-scale bedforms. Here, as discussed in the introduction, we apply a logarithmic friction law to parameterize roughness effects. *Prandtl* [1926] showed from theoretical analysis that, under the velocity-gradient assumption and in the zone immediately above a very thin viscous sublayer, the time-averaged velocity (u) varies as a logarithmic function of distance from the wall, the so-called law of the wall:

$$\frac{u}{u^*} = \frac{1}{\kappa} \ln \frac{z}{z_0}, \tag{1}$$

where z is the distance from the wall, κ is the von Kármán constant (0.4), u^* is the shear velocity, and z_0 is a characteristic length scale. Through a series of experiments in pipes coated with sand grains of uniform diameter, *Nikuradse* [1933] showed that (1) z_0 could be interpreted as a function of the average projection of individual grains; (2) for his experiments, the grain projection could be taken as the diameter (D) of the sand grains used, which Nikuradse labeled k; and (3), as a result of experimental analysis, z_0 was approximately $k/30$. In equation (1), the velocity at $z = z_0$ is zero, which is effectively a hydraulic outward projection of the bed. In the present analysis, this equation is used to specify the bed shear stress using a source term in the discretized momentum equations for cells next to the bed.

[19] In this paper, bed shear stress is parameterized using the log-law as defined in equation (1), with the roughness length specified as uniform across the domain. This implies that the roughness elements are uniform throughout the reach. However, bedform roughness is likely to be spatially distributed [*Nicholas*, 2005; *Zeng et al.*, 2008, *van Balen et al.*, 2010] and typically scales with flow depth. A uniform increase in roughness length is therefore likely to increase flow routing into deeper areas of the reach. Thus, to calibrate and test the sensitivity of the model to roughness, we ran a series of simulations where the roughness length was changed systematically.

[20] *Colebrook and White* [1937] obtained a version of equation (1) that represented the mean flow by evaluating the area integral of equation (1) across, in their case, a pipe. A form of this equation is often used in depth-averaged simulations, where equation (1) is integrated over the entire depth and the *Nikuradse* [1933] pipe flow roughness length k_s (=30 z_0) is applied:

$$\frac{U}{u^*} = \frac{1}{\kappa} \ln\left(\frac{30\phi h}{k_s}\right), \tag{2}$$

where U is the depth-averaged velocity, $\phi \approx \exp(-1)$, and h is the depth. This equation is often referred to as a Colebrook-White "type" equation [e.g., *van Rijn*, 1984; *Paarlberg et al.*, 2010] in recognition of their work on flow in pipes (hereafter referred to as CWE). The assumption here is that the velocity is log-linear over the entire flow depth. Deviations in this velocity profile lead to differences in resultant shear stress estimates between depth-averaged

and 3-D applications for a given roughness length. Therefore, the application of a roughness-length derived for depth-averaged applications may not be directly applicable. The present paper tests these relationships by computing the roughness lengths applied with those that would be obtained if equation (2) was applied. Details of this analysis are given in section 3.3.

[21] To estimate the likely range of roughness lengths, we used this equation (equation 2) specifying the reach-averaged bed shear stress using: $\tau_w = \rho g h S$, where S is the water surface slope ($\sim$4.4 cm km^{-1} for this reach of the Rio Paraná). This resulted in a relationship between roughness length, depth-averaged velocity, water surface slope, and depth. From analysis of the topographic data, the average and minimum traverse cross-sectional areas (A_{cs}) are approximately 16,000 m^3 and 13,000 m^3. The mean and maximum transect-averaged velocities (Q/A_{cs}) are therefore: 0.9 and 1.2 m s^{-1}. Furthermore in the studied reach, the mean and maximum depths are 5.7 and 26 m, respectively. Using relationship just discussed and estimates for water surface slope, depth, and velocity, a range of roughness values was obtained. The largest ($k_s = 3.0$ m) and lowest ($k_s = 0.003$ m) roughness lengths in this range were obtained by using the maximum ($h = 26$ m) and reach-averaged ($h = 5.7$ m) depths, respectively. Both largest and lowest roughness lengths were estimated by using the maximum transect-averaged velocity ($U = 1.2$ m s^{-1}). An intermediate roughness length ($k_s = 0.04$ m) was obtained using the average depth ($h = 5.7$ m) and average transect-averaged velocity ($U = 0.9$ m s^{-1}); this is perhaps more representative of the entire reach. We also evaluated the sand roughness based on grain size and on the averaged dune scales. There are a number of formulations that relate sand roughness k_s to the sediment size by: $F_s D_{rep}$ [e.g., *Mahmood*, 1971; *Kamphuis*, 1974; *Hey*, 1979a; *van Rijn*, 1984] (see *Garcia* [2006] for a comprehensive list), where F_s is a scaling factor in the range 1–6.6 and D_{rep} is a representative grain size that is typically the 80–90 percentile. The Río Paraná is a sand bed river, and our measurements suggest that $D_{50} = 350$ μm, and so typical sand roughness is of the order 0.001 m. To estimate the effect of bedforms, we used the *van Rijn* [1984] roughness predictor. With the typical dune height and length around 1.5 m and 64 m, respectively, the form-induced roughness is 0.73 m. *van Rijn* [1984] suggested that the total effect of the grain- and bedform-scale roughness can be computed as the linear summation of these effects. Since the bedform term is much more dominant, $k_s \sim 0.73$ m. Based on this analysis, we selected roughness lengths in the range: 0.0003–3 m.

2.4. Computational Fluid Dynamics

[22] The hydraulics of open-channel flow are governed by a set of conservation laws for mass and momentum (the Navier Stokes equations). In this paper, we investigate the time-averaged flow field and so implement a numerical scheme to solve the Reynolds-averaged Navier Stokes equations in Cartesian space (x, y, and z). This set of equations can be written in tensor form as follows:

$$\sum_{j=1}^{3} \frac{\partial u_j}{\partial x_j} = 0, \tag{3}$$

$$\sum_{j=1}^{3} u_j \frac{\partial u_i}{\partial x_j} = -\frac{1}{\rho}\frac{\partial p}{\partial x_i} + \sum_{j=1}^{3} \frac{\partial}{\partial x_j}\left(\nu_m \frac{\partial u_i}{\partial x_j} - \overline{u_i' u_j'}\right) + g_i, \tag{4}$$

for $i = 1, 2, 3$ (x, y, z), where u is the time-averaged velocity, u' is the turbulent velocity fluctuation (relative to the time-averaged), p is pressure, ρ is the fluid density, ν_m is the fluid molecular kinematic viscosity, g_i is the gravitational acceleration constant ($g_1 = g_2 = 0$ and $g_3 = g$), and $\overline{u_i' u_j'}$ is the Reynolds stress (a product of time averaging the Navier Stokes equations).

[23] These equations are not closed since the Reynolds stress terms $\overline{u_i' u_j'}$ cannot be computed directly, and so a suitable turbulence model is required. The simplest complete turbulence model that does not require the specification of turbulent structure is provided by two-equation closure schemes [*Sotiropoulos*, 2005], such as the linear κ–ε turbulence model. However, the underlying assumption of these types of models is that turbulence is isotropic and therefore they do not predict anisotropic, turbulence-driven, secondary circulation [*Einstein and Li*, 1958]. To include this process, it is necessary to use higher-order models such as nonlinear κ–ε models [*Speziale*, 1987], algebraic stress models [*Martinelli and Yakhot*, 1989; *Launder and Ying*, 1973] and Reynolds stress transport models (RSTM) [*Launder et al.*, 1975].

[24] The RSTM offers the most theoretically correct approach to predict anisotropic turbulence, as the Reynolds stresses are computed directly without evoking the Boussinesq eddy-viscosity hypothesis. To compute these stresses, the RSTM involves seven additional transport equations for a three-dimensional problem. These are second-order closure models that are potentially superior to the simpler eddy viscosity models [*Ingham and Ma*, 2005]. However, the limitation of RSTMs is their complex formulation, which makes them difficult both to implement and ensure numerical convergence [*Sotiropoulos*, 2005], especially over complex topography. Furthermore, they are computationally more expensive [*Ingham and Ma*, 2005], and it is reported that not all fluid flow simulations benefit from this model, particularly when fluid flows are straining [*Rodi*, 1993]. Finally, there is a practical limit to the use of the RSTM at the same time as the mass-flux scaling algorithm, since both models require the use of the same storage algorithm in our current version of the code. However, the mass-flux scaling algorithm (see below) is critical to representation of topography and hence topographically - induced secondary circulation. Laboratory and field data show that turbulence-driven secondary circulations are typically small (up to 2% of the primary flow velocities, *Nezu and Rodi* [1985]; *Onitsuka and Nezu* [2001]), and the principal mechanism for flow velocity redistribution is topographically induced secondary circulation that dominates over both inertia and secondary flows [*Blanckaert*, 2010].

[25] Our priority was effective topographic representation using the mass-flux scaling algorithm, rather than turbulence representation using the RSTM. Therefore, in the present paper, we apply a two-equation κ–ε turbulence model modified using renormalization group theory (RNG) [*Yakhot et al.*, 1992]. This model has been shown to outperform the standard κ–ε turbulence model in areas of flow separation and reattachment [*Yakhot et al.*, 1992;

Lien and Leschziner, 1994a; *Dargahi*, 2004]. The linear κ–ε model uses the Boussinesq eddy-viscosity hypothesis, which states the Reynolds stress terms can be approximated as

$$-\overline{u_i' u_j'} = \nu_t \left(\frac{\partial u_i}{\partial x_j} + \frac{\partial u_j}{\partial x_i} \right) - \frac{2}{3} k \delta_{ij} \tag{5}$$

where δ_{ij} is the Kronecker delta ($\delta_{ij} = 1$ if $i = j$, otherwise $\delta_{ij} = 0$) and $k \left(= \frac{1}{2}\left(u'^2_1 + u'^2_2 + u'^2_3 \right) \right)$ is the turbulent kinetic energy [cf. *Versteeg and Malalasekra*, 2007]. Closure of equations (3)–(5) was achieved using a κ–ε RNG turbulence model, whereby the turbulent viscosity $\nu_t \left(= c_\mu k^2/\varepsilon \right)$ is computed from the turbulent kinetic energy, k, and turbulent dissipation, ε. These are obtained by solving their own scalar transport equations:

$$\frac{\partial (k u_i)}{\partial x_i} = \frac{\partial}{\partial x_j} \left[\frac{\nu_t}{\sigma_k} \frac{\partial k}{\partial x_j} \right] - P_k - \varepsilon, \tag{6}$$

$$\frac{\partial (\varepsilon u_i)}{\partial x_i} = \frac{\partial}{\partial x_j} \left[\frac{\nu_t}{\sigma_k} \frac{\partial \varepsilon}{\partial x_j} \right] + \frac{\varepsilon}{k} (C_{1\varepsilon} P_k - C_{2\varepsilon} \varepsilon), \tag{7}$$

where

$$P_k = \overline{u_i' u_j'} \left(\frac{\partial u_j}{\partial x_i} + \frac{\partial u_i}{\partial x_j} \right), \tag{8}$$

is the production of turbulent kinetic energy through shear, $c_\mu = 0.0845$, $\sigma_k = \sigma_\varepsilon = 0.7194$, $C_{1\varepsilon} = 1.42$, and

$$C_{2\varepsilon} = 1.68 + C_\mu \eta^3 \frac{1 - \eta/4.38}{1 + 0.012\eta^3}, \tag{9}$$

are constants determined experimentally, and $\eta \left(= k\sqrt{P_k/\nu_t}/\varepsilon \right)$ is a dimensionless parameter [*Yakhot et al.*, 1992].

[26] Solution of these equations was obtained using a modified version of a finite volume code, PHOENICS copyright, which includes a range of options for numerical discretization and solution (e.g., boundary fitting of coordinates; multiblock solutions). PHOENICS offers the flexibility to edit and recompile subroutines that can be included at runtime. This code was modified by introducing a mass-flux scaling method to represent variations in riverbed morphology in a structured grid solution, without the need for boundary-fitting grids in ways that can lead to high levels of numerical diffusion or instability [*Lane et al.*, 2004; *Hardy et al.*, 2005, 2006]. The method uses a numerical porosity treatment, similar to *Olsen and Stokseth* [1995], who used a structured grid with specified cell porosities to block out the bottom topography: $Pf = 1$ for cells that are all water; $Pf = 0$ for cells that are all bed; and $0 < Pf < 1$ for partly blocked cells. *Lane et al.* [2004] developed and validated the method for high-resolution applications (representation of individual gravel particles with a grid resolution of 0.002 m), including the introduction of appropriate drag terms into the momentum equations. *Hardy et al.* [2006] applied the method to a 1.8 km × 0.25 km dune field in the Río Paraná but used a more sophisticated treatment, with a five-term porosity algorithm that included four vertical faces of the cell and the cell volume rather than a single scaling (porosity) term. In this paper, we apply this method within the framework of a structured Cartesian grid to represent bed topography. In the representation of complex bed geometries, this method is much more stable and leads to less numerical diffusion than boundary-fitted methods [*Lane et al.*, 2004].

[27] Pressure was computed using the Semi-Implicit Method for Pressure-Linked Equations SIMPLE [*Patankar and Spalding*, 1972] algorithm, and the second-order upstream monotonic interpolation for scalar transport (UMIST) differencing scheme [*Lien and Leschziner*, 1994b] was employed to compute convective terms. A rigid-lid approximation was applied at the free surface, introducing an additional surface-pressure term, but necessitating a mass correction of the surface-adjacent cells [*Bradbrook et al.*, 2000]. This correction is particularly important because changes in roughness may influence flow depth. Changes in pressure on the lid represent such changes implicitly but may lead to violation of conservation of mass.

[28] The ADCP data from cross-section CS-A (Figure 1d) were used to orientate the DEM relative to the computational mesh; y and z were parallel to, and x perpendicular to, the cross section (Figure 1d). These velocity data were then used to specify the inlet boundary condition using a fixed-mass boundary with 5% turbulence intensity specified. The outlet was defined on the downstream end of the domain using a fixed-pressure boundary condition but where mass is allowed to enter and leave the domain. Bed shear stress was computed assuming an equilibrium boundary, and so the near-bed kinetic energy $k \left(= u^{*2}/\sqrt{C_\mu} \right)$ and dissipation $\varepsilon \left(= C_\mu^{3/4} k^{3/2}/\kappa \Delta z_p \right)$were fixed using source terms in the respective discretized transport equations. Here, Δz_p is the distance between the bed and the near-bed cell center. The resulting bed shear stress was computed using equation (1) with a roughness length specified using the Nikuradse sand roughness length:

$$\tau_{w,i} = \rho \left(\kappa / \ln \left(30 \Delta z_p / k_{\mathrm{sM}} \right) \right)^2 u_r u_i \tag{10}$$

where $u_r \left(= \sqrt{u_1^2 + u_2^2} \right)$ is the magnitude of the resultant velocity near the bed, $\tau_{w,i} \left(= \rho u^{*2} \right)$ is the bed shear stress, and k_{sM} is the modeled roughness length. This shear stress enters the momentum equation as a source term, applied to cells next to the bed (see *Versteeg and Malalasekra* [2007] for further details).

[29] To determine suitable cell dimensions, a grid convergence index [GCI, *Hardy et al.*, 2003] test was used to explore mesh dependence. The GCI method involves a series of grid refinements where the finite volume dimensions are reduced by a factor of 2, with at least three domains used to assess the solution convergence. In these simulations, the mesh size was set to 15 m in the horizontal plane (Δx and Δy) and 1 m in the vertical direction (Δz). Following *Casas et al.* [2010], the required roughness values would be expected to change with mesh size, but the focus here is on roughness representation for a given mesh size. Using these cell dimensions, the domain was constructed from 775 cells in the x direction, 297 cells in the y direction, and 26 cells in the z direction. It is not possible to look for mesh independence in an irregular topography because refining the

mesh results in changes in the resolved topography. As the mesh is made finer, flow is resolved around elements that relate to how the topography was sampled [*Casas et al.*, 2010]. To eliminate this effective change in bed topography, GCI tests were conducted on a mesh that did not contain any bed topography. The mean GCI between the two highest resolution meshes was 1.02% for the downstream (u_x) component, 5.51% for the cross-stream (u_y) component, and 5.13% for the vertical (u_z) component, demonstrating minimal effect of the grid resolution on the prediction of the hydraulics. It is therefore appropriate to assume that the simulations performed on this resolution were grid independent.

[30] These tests were conducted specifying the same wall treatment in each case and thus the effect of spatially variable roughness length has not been assessed. In this paper, we investigate the response of the model to the application of a range of roughness lengths from 0.003 to 3 m. The effect of changing the roughness length is to increase the bed shear stress, which produces larger velocity gradients near the bed. To fully resolve these velocity gradients, it may therefore be necessary to reduce the vertical resolution as roughness is increased. However, our GCI tests were conducted for $k_{sM} = 1.50$ m, which covers the lower half of the assessed roughness length range. As we will show in the following section, the optimal solution is obtained in this lower range of values. Furthermore, there is a theoretical limit on the feasible mesh length scales that is associated with the physical meaning of roughness length z_0 ($=k_s/30$) in equation (1). That is, at z_0 above the bed the flow velocity is zero, and is essentially a hydraulic outward projection of the bed. Therefore, since equation (1) is applied at the cell center: $0.5\Delta z \geq z_0$. There is also a practical constraint associated with computing flows in large rivers that limit the size of the grid cells used. In this paper, we have maximized the grid cell size to resolve a reach that contains: (1) ADCP data to inform model boundary conditions at cross-section CS-A and model assessment at cross-section CS-B (see Figure 1d), and (2) a region of convergent flow (around the large bar in Figure 1). This approach was taken to (1) assess the model predictions and (2) investigate typical flow fields in a confluent area of the reach, which exhibit circulatory flow patterns.

3. Results

3.1. Model Predictions, Model Observations, and Roughness Length

[31] In this section, we assess the performance of the model using a number of metrics to compare model solutions with field measurements, including reach-averaged water surface slope and measured velocity. Calibration of numerical models of fluvial flows typically use the water surface slope to parameterize energy losses. However, for rivers with small water surface slopes such as the Río Paraná [O(10^{-5}): *Szupiany et al.*, 2007; *Ramonell et al.*, 2002], this slope is difficult to measure accurately [*Latrubesse*, 2008]. For the reach investigated herein, a large range of values have been cited from 3 to 8.5 cm km^{-1} [*Orfeo and Steveauz*, 2002; *Drago and Amsler*, 1998; *Latrubesse*, 2008; *Nicholas et al.*, 2012].

[32] Figure 3 presents the water surface slope as a function of the roughness length applied and reveals that the water surface slope varies significantly (2.9–16 cm km^{-1}) over the roughness lengths simulated. As the roughness length is increased, there is a relatively rapid nonlinear increase in water slope until $k_{sM} = 0.3$ m. For larger roughness lengths, the rate of increase slows and becomes more linear. This indicates that the model is more sensitive in terms of changes in water surface slope to smaller roughness lengths. For the range of water surface slopes measured in this reach of the Río Paraná (3–8.5 cm km^{-1}), the optimal roughness length is between 0.005 and 0.63 m. However, our estimate of the water surface slope is 4.4 cm km^{-1} [*Nicholas et al.* 2012], and this gives an optimal roughness length between 0.03 and 0.06 m.

[33] With all the uncertainty associated with measurements in water surface slope, it is preferable to optimize the model using velocity data. To make the comparison between the model and measured velocity data, each data point from cross-section CS-B (Figure 1d) is represented by spatially averaging the ADCP data within each CFD control volume. This leads to a mean velocity observation for that CFD volume, as well as an uncertainty estimate based upon the standard deviation of velocities recorded in that CFD volume for all repeat transect ADCP surveys. The *x*-directed and *y*-directed components of the measured velocity were then rotated to project them into the Cartesian frame of reference used in the CFD model.

[34] Figure 4 compares the averaged ADCP measurements with model predictions for each component of velocity, u_x, u_y, and u_z, and for each velocity point and component provides an error bar based on the uncertainty estimate. The model predictions are presented for four values of roughness length (0.015, 0.15, 0.30, and 3 m).

[35] To quantify the level of agreement between measurements and predictions for each roughness length, it is important to consider both (1) the degree of scatter in the

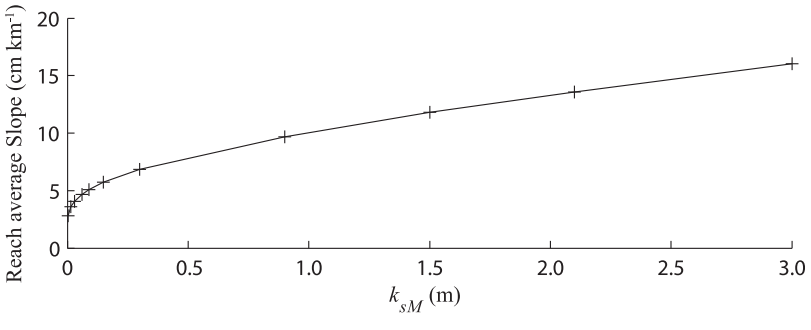

Figure 3. Reach-averaged water surface slope as a function of applied roughness length.

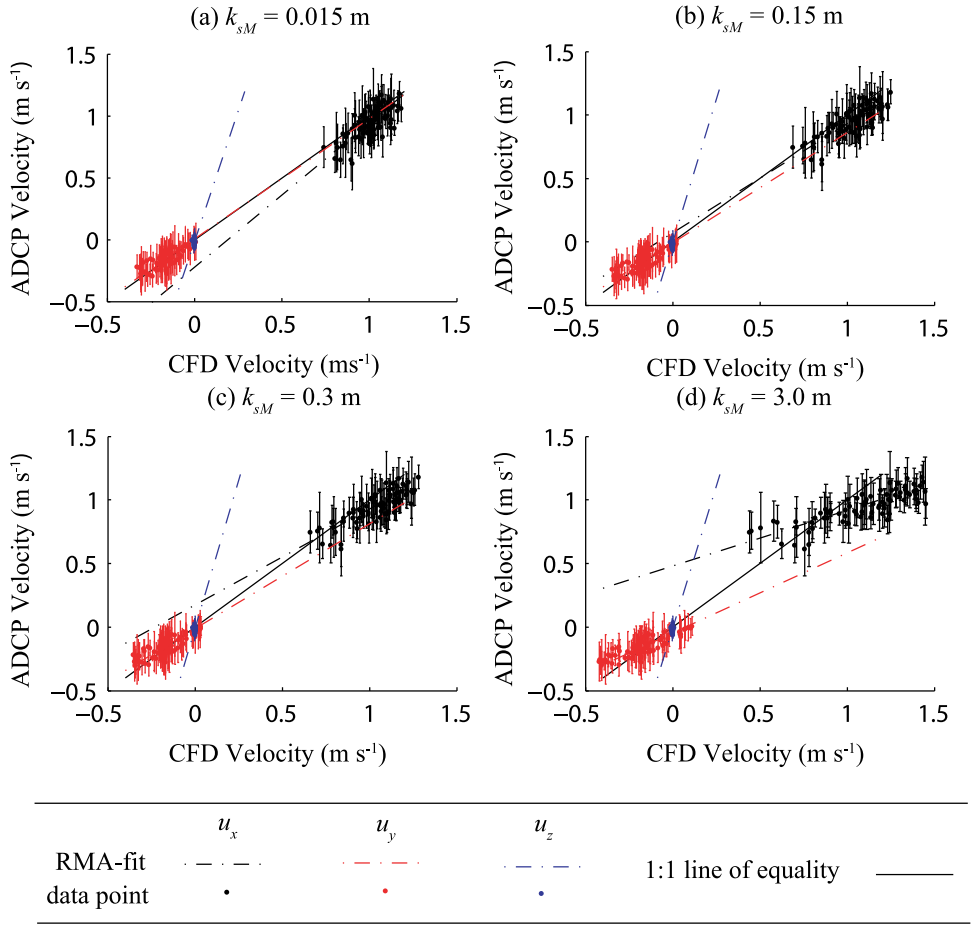

Figure 4. Comparison between measured ADCP and predicted CFD velocities. The solid line represents the 1:1 line of equality while the dot-dashed line shows a RMA least-squares regression applied to each data set. Each component of velocity is presented and, for clarity, only every tenth data point is plotted.

data and (2) the degree of bias. This was analyzed using (1) the correlation coefficient r and (2) the gradient m obtained from reduced major axis (RMA) regression, the latter being selected to reflect the fact that uncertainty is expected in both the predicted and the observed data [see *Hardy et al.*, 2003]. Herein, two additional statistics are also determined: (3) the variance (σ^2) of data points around the 1:1 line of perfect equality; and (4) the percentage of predicted velocities within one, two, and three standard deviations of the measured ADCP data. These results are presented in Figures 5 and 6.

[36] Figure 5 provides quantitative summaries of the level of (1) bias and (2) scatter for each component of velocity for all the roughness lengths simulated. Both Figures 4 and 5 show that the level of agreement between observations and predictions is more sensitive for u_x than for u_y, and for u_y than for u_z. This is not surprising, because the magnitude of the bed shear stress when integrated across the boundary cell scales with the square of velocity and generally $u_x > u_y > u_z$. Figure 5a shows the slope estimates obtained using RMA linear regression. Those for u_z deviate significantly from unity between $m = 4.10$ and $m = 4.82$ (although not shown for clarity), and this is accompanied by nonsignificant correlation values (Figure 5b). Inspection of Figure 6 shows that this is primarily because the relative error for the ADCP u_z values is much greater than those for u_x and u_y: the ADCP contains significant variability in vertical flow velocities that is not captured by the resolution at which this model is being applied. This is not surprising given that the ADCP data include the effects of significant bedforms (i.e., dunes, with a typical normalized height of $b_a/h = 0.35$, where b_a is bedform amplitude and h is local flow depth) that are not represented in the model domain. For u_z, changing the roughness length has very little impact upon the level of agreement, whether in terms of slope or correlation (Figure 5), and uniform roughness-length variation cannot be used as a means of calibrating the model on vertical-velocity measurements. This problem might be resolved with higher-resolution topographic data that could be used to specify some localized spatial variability in roughness length, but acquiring data at such high resolutions over very long reaches of wide rivers may be prohibitively time consuming, unless it becomes possible using remotely sensed techniques.

[37] The results for u_x and u_y are more encouraging for two reasons. First, both the gradient m (Figure 5a) and correlation coefficient r (Figure 5b) values are much better than those obtained for u_z. They also show, as noted above,

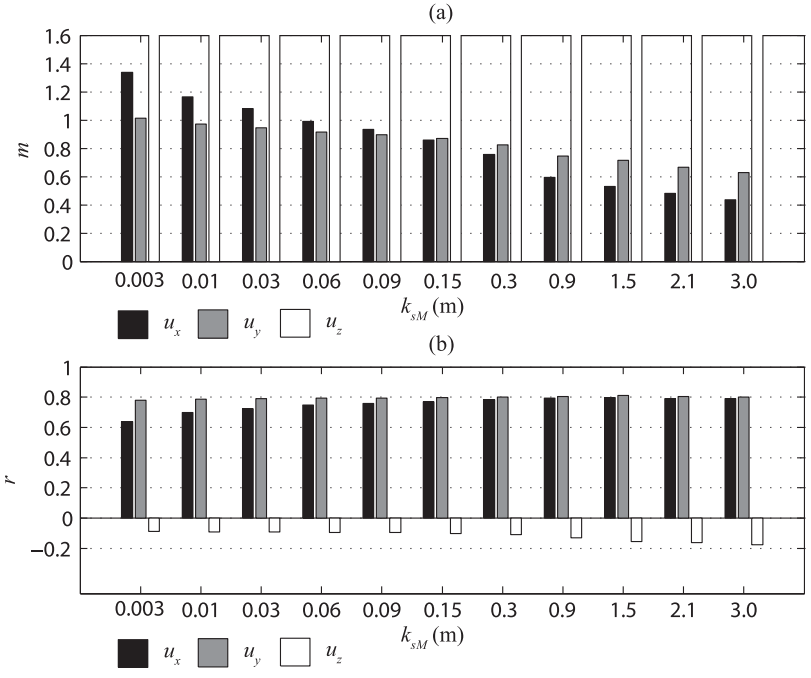

Figure 5. (a) Gradient m obtained from RMA least-squares regression and (b) correlation coefficient r for all three components of velocity. The gradient terms for u_z are very large (4.06–4.88), and so, for clarity, they have been limited to between 0 and 1.6. Also included in this figure is the reach-averaged slope as a function of simulated roughness length. (c) Reach-averaged water surface slope as a function of the applied roughness length.

a sensitivity to roughness length. However, it is also clear that the roughness length that optimizes the fit of model predictions to observations varies with the statistic considered (bias versus scatter) and, to a lesser extent, with velocity component (Figure 5). Thus, bias is minimized in u_x at $k_{sM} = 0.06$ m and in u_y at $k_{sM} = 0.003$ m, although the latter significantly increases the bias in u_x (Figure 5a). However, scatter in u_x and u_y is minimized at $k_{sM} = 3.0$ m, but with little variation in scatter between $k_{sM} = 3.0$ m and $k_{sM} = 0.90$ m (Figure 5b). The optimal agreement for bias is at the lower roughness lengths simulated, and the optimal agreement for scatter is at the higher roughness lengths

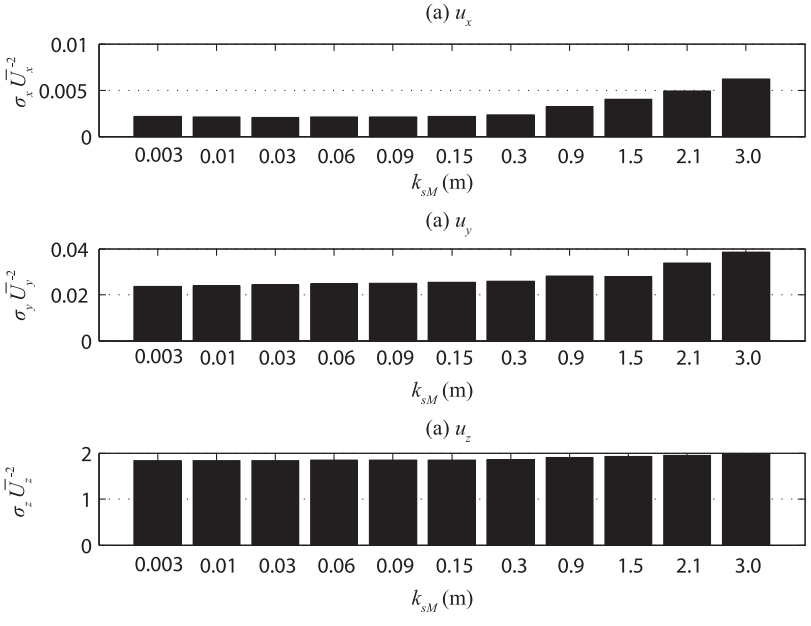

Figure 6. (a–c) Variance about the 1:1 line of equality for all three components of velocity. Note the different scale for each component.

simulated. Inspection of Figure 4d suggests that the scatter statistic (correlation coefficient r) is somewhat misleading. Even though the results for this roughness length (k_{sM} = 3.0 m) exhibit the least scatter (Figure 5b), the associated gradient is far from unity (Figure 5a). Taken together, it appears that optimal results are obtained using k_{sM} = 0.06 m for u_x with a correlation coefficient of 0.62, and k_{sM} = 0.003 m for u_y with a correlation coefficient of 0.75.

[38] Estimates of the errors between measured and predicted results are presented in Figure 6 for each velocity component and roughness length applied. In each case, the difference between the velocity pair (measured and predicted) and the 1:1 line of equality was calculated. These residual values were then used to calculate the variance. This was then normalized using the square of the mean measured velocity for the entire cross section $\overline{U}_x$, $\overline{U}_y$, and $\overline{U}_z$, which are of the order 1, 10^{-2}, and 10^{-3}, respectively. Figure 6 is valuable in identifying which values of roughness minimize errors. For all three components, the variance is minimized for lower roughness lengths and in general is largely invariant for $k_{sM} < 0.30$ m.

[39] Finally, Figure 7 shows a comparison between the (a) ADCP and (b–d) CFD velocity profiles using filled contour plots of the velocity magnitude. The measured flow (Figure 7a) is characterized by a number of higher-velocity flow cores where the velocity magnitude peaks locally. The results show that these flow patterns occur across the entire cross section and extend approximately 100 m laterally. The measured results also show that the maximum measured velocity is located in the deeper part of the channel (S = 500 m). Similar flow patterns are observed in the CFD results (Figures 7b–7d) although the lateral extent of the higher-velocity flow cores is larger. These flow patterns are likely driven by upstream topographic forcing. The predicted flow patterns are much more diffuse compared with the measured flow, suggesting that finer-scale topography that is missing in the model may be important in determining spatial flow patterns. Comparison between the model results also shows that increasing the roughness (b–d) leads to more flow being routed into the deeper channels.

[40] In this analysis, we have used a number of statistical measures in an attempt to elucidate optimal roughness lengths. Taken together, it appears that the best fits between observations and predictions are obtained for lower values of roughness length. However, it is also clear that roughness length is not an effective means of compensating for the effects of the bedforms associated with this river. Roughness length certainly does not represent the effects of bedforms on u_z, and simply upscaling k_{sM} does not appear to capture the effects of bedforms on u_x or u_y. The most sensitive statistics appear to be bias (the gradient of the line obtained using RMA regression) and scatter (the correlation coefficient r). This thus suggests that optimization based on the correlation coefficient alone could be misleading, and

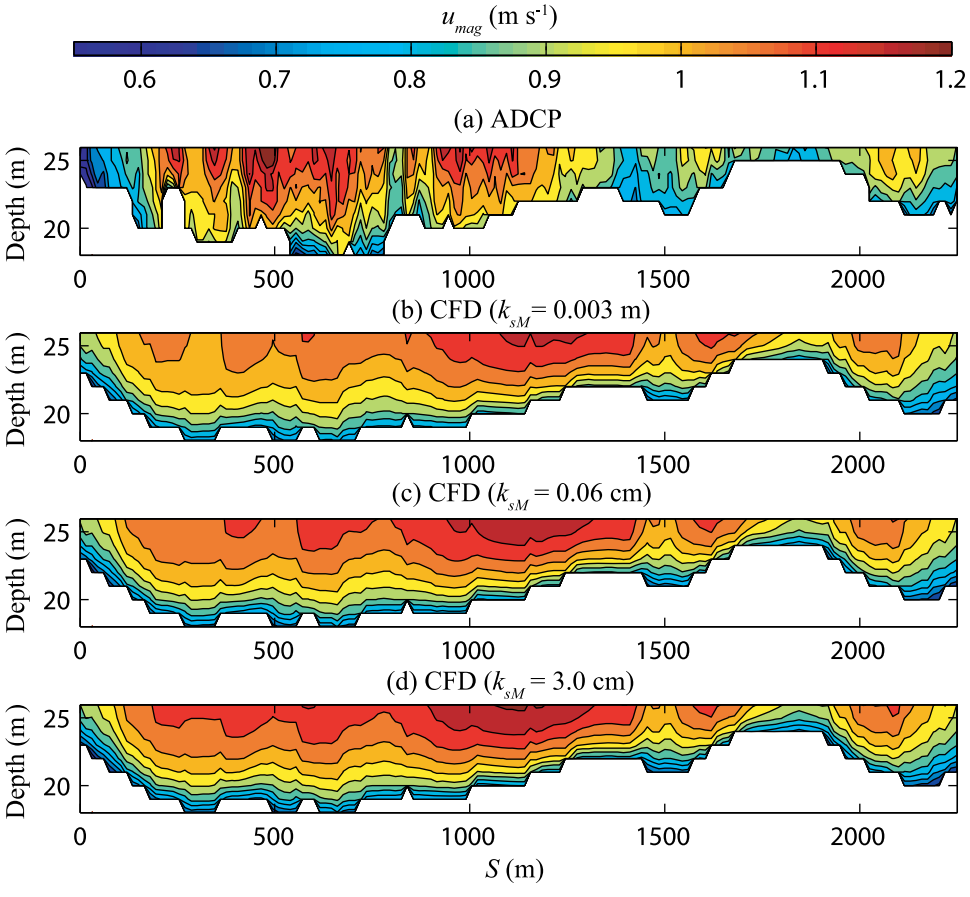

Figure 7. Spatial pattern of velocity magnitude in cross section B for (a) ADCP measurements, (b) model with k_{sM} = 0.003 m, (c) model with k_{sM} = 0.06 m, and (d) model with k_{sM} = 3.0 m.

that the optimal results obtained are for the simulations where $k_{sM} = 0.06$ m for u_x and $k_{sM} = 0.003$ m for u_y.

[41] Since u_x and u_y largely represent the streamwise and cross-stream flow directions, respectively, and k_{sM} includes form roughness effects that have a larger impact in the streamwise direction, it is not surprising that the optimal roughness length is more sensitive for the u_x velocity component and different to the optimal roughness length for the u_y velocity component. Since the optimal results based on the water surface slope and the x-directed velocity (u_x) are around $k_{sM} = 0.03$–0.06 m, we use the results obtained for $k_{sM} = 0.06$ m to present the primary and secondary flow in a series of cross sections in section 3.4.

3.2. Roughness Length and Sensitivity to Flow Routing

[42] In complex multithread channels, uniform changes in bed roughness have been found to create complex and sometimes counterintuitive impacts on flow velocity [e.g., *Lane et al.*, 1994]. For example, in a 2-D-numerical-modeling study of a multithread gravel-bed river, *Lane et al.* [1994] found that uniform increases in bed roughness resulted in flow deceleration in shallower zones, but, because of roughness submergence effects, and so as to conserve mass, flow velocity increased in deeper zones where roughness was more submerged. Such effects have not been explored in large rivers. To investigate the influence of roughness on flow routing, a deeper (Channel A, Figure 2, clear thalweg, ~15 m depth) and a shallower (Channel B, Figure 2, ~5 m depth) channel was identified, and predicted velocity profiles (labeled P_a and P_b in Figure 2) were extracted from each to assess their sensitivity to the roughness lengths employed.

[43] In Figures 8a and 8b, these velocity profile predictions are presented for each roughness length simulated. Also included in these figures are the reconstructed velocity profiles obtained through the application of the CWE (equation (2)). The results show that, in all cases, increasing the roughness length results in a reduction in the near-bed velocity. In the shallower channel (Figure 8b), this effect extends throughout the flow depth for most roughness lengths. However, in the deeper channel (Figure 8a), this effect is limited to the bottom 20% of the flow depth, with the upper part of the flow column exhibiting large increases in flow velocity in response to the increase in roughness length. This is more clearly seen in Figure 8c, which compares the predicted near-surface and near-bed velocities (at 95% and 5% of the local flow depth, respectively) as a function of roughness length. The sensitivity of near-bed velocities to changes in roughness length is similar in both channels, but the sensitivity of near-surface velocities is much greater in the deeper channel, especially for small changes in roughness length.

[44] Assessment of how the discharge ratio between channels A and B ($Q_R = Q_B/Q_A$) changes as a function of k_{sM} shows that the increase in velocity for $z/h > 0.2$ is associated with an increased discharge in channel A (Figure 8d). Figure 8d shows how the flow is routed as the roughness is changed. The results show that, for low roughness lengths,

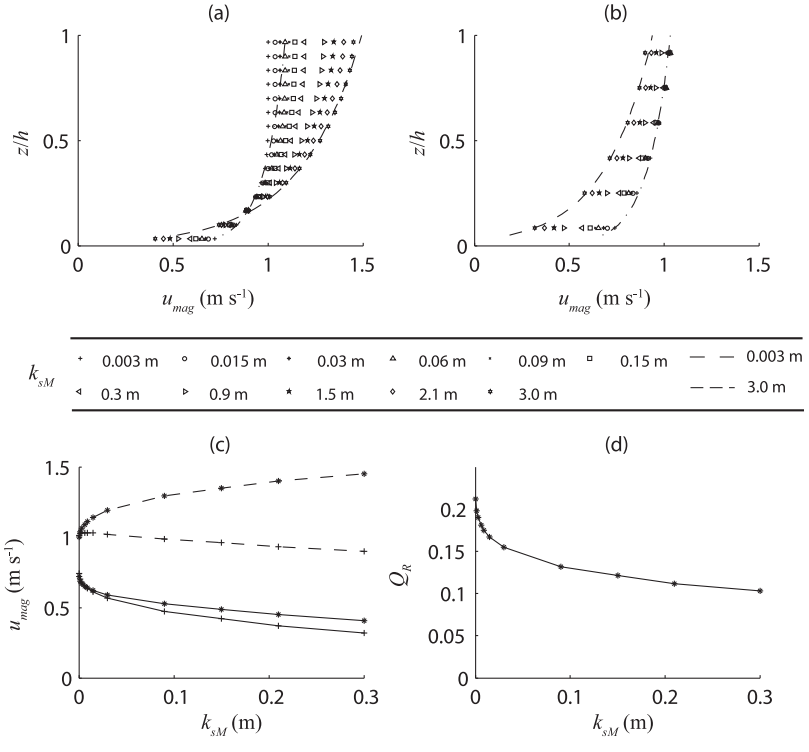

Figure 8. Velocity profiles extracted from the CFD domain at (a) $x = 5.8$ and $y = 2.1$ km (P_a) and (b) $x = 6.8$ and $y = 3.6$ km (P_b) for various uniform boundary roughness lengths (0.003–3.0 m). Also shown are the CWE fits to the inferred $k_{s,inf}$ values and depth-averaged velocities. (c) Near-bed (solid line) and near-surface (dashed line) velocity for the profiles presented in Figure 8a (filled circles) and 8b (+). (d) Discharge ratio Q_R ($= Q_B/Q_A$) as a function of roughness length ($Q_{tot} = 15{,}100$ m^3 s^{-1}).

approximately 20% of the flow is routed down the shallower channel, while for the largest roughness length, the total flux drops by around 50% of the previous value to around 10% of the total flow. In fact, the model is most sensitive for smaller roughness lengths, whereby nearly half of the changes in discharge ratio occur for the smallest 20% of simulated roughness lengths. The results shown in Figure 8 are important, because they show that even small changes in roughness length, a parameter that was found to be difficult to calibrate reliably given the available flow-measurement data, can have a major impact upon the way that flow is routed through the channels. These kinds of extreme sensitivity are likely to result in a high probability of divergence between predicted model behavior and observed river behavior in models of form-flow-sediment transport feedback [*Haff*, 1996] and will be further complicated by the effects of spatial variability in bed roughness [*Nicholas*, 2005].

3.3. Reinterpreting Roughness Lengths in CFD Simulations of Large Rivers

[45] The previous sections have shown a marked sensitivity of flow routing and flow structures to changes in roughness length as well as no clear means by which a global roughness-length value might be optimized based on observations. A primary reason for this sensitivity appears to be the effects of changes in roughness length on flow routing, such that roughness length responses cannot be described by local parameterizations alone. It is almost certainly the case that roughness representation needs to move away from a focus upon grain upscaling to incorporate the wider set of influences upon energy losses (e.g., flow convergence and divergence). Additionally, there is also the uncertainty caused by the known discrepancy between the spatial resolution, and hence, the associated topographic data content of the model used herein, and the features of bed topography (e.g., dunes) present in large rivers such as the Río Paraná. In this part of the paper, we explore how the problem of roughness representation in 3-D and 2-D CFD simulations of large rivers can be addressed from analysis of model data extracted from 3-D simulations.

[46] The velocity profiles shown in Figures 8a and 8b are plotted in log-linear space in Figures 9a and 9b for the smallest and largest roughness lengths simulated (k_{sM} = 0.003 m and k_{sM} = 3.0 m). These plots show a clear log-linear relationship that holds from near the bed and through a significant proportion of the flow depth, extending through almost the entire flow depth in the shallower channel (Figure 9b). These results show that the velocity profile is log-linear over a larger portion of the depth for (1) velocity profile P_b and (2) increasing roughness lengths. In this paper, this portion of the flow is referred to as the log-linear layer. This method has been used before to estimate bed shear stress and roughness lengths in rivers [e.g., *Ashworth and Ferguson*, 1986; *Ashworth et al.*, 1992; *Whiting and Dietrich*, 1991; *Wiberg and Smith*, 1991; *Biron et al.*, 1998].

[47] Using linear regression, a function of the form $u_{mag} = a \ln(z) + b$ was fitted to the data in the log-linear region.

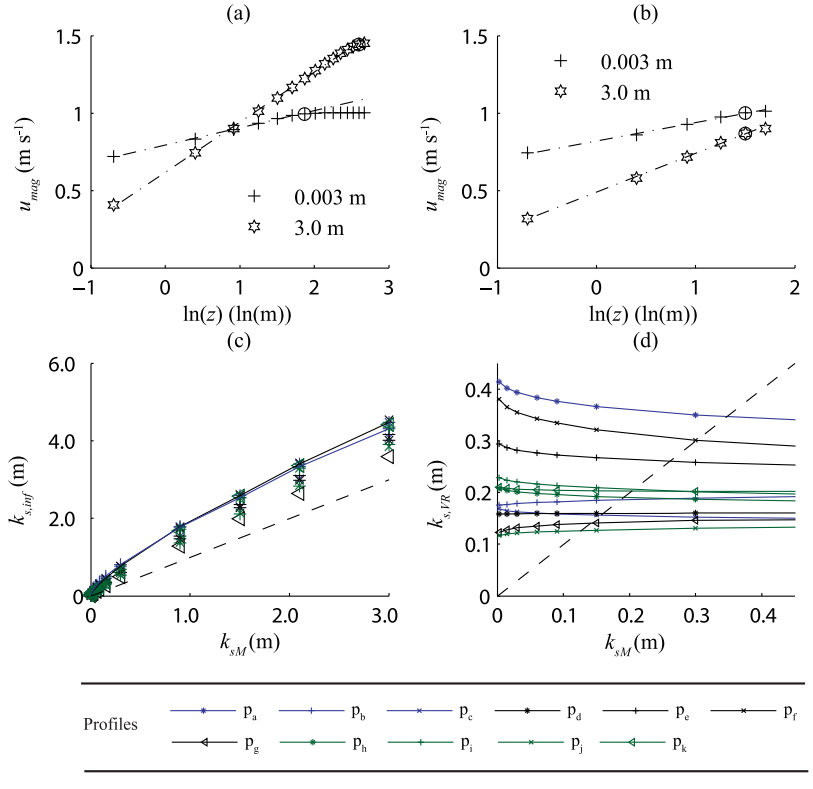

Figure 9. Log-linear velocity profiles at (a) x = 5.8 and y = 2.1 km (P_a) and (b) x = 6.8 and y = 3.6 km (P_b) for k_{sM} = 0.003 and 3.0 m. (c) Equivalent roughness length $k_{s,inf}$ plotted as a function of roughness length k_{sM}. (d) The roughness length computed from the simulated results using the *van Rijn* (2007) parameterization.

These fitted lines are plotted in Figures 9a and 9b (dotted lines) together with the velocity predictions. The data included in this regression extends from close to the bed, up to and including the data points that are encircled. The depth of the log-linear layer is dependent on the roughness length, extending further into the flow for higher values of k_{sM}. As the profiles are not log-linear over the entire flow depth, it was necessary to restrict the fit to the zone displaying a log-linear behavior. This was undertaken by increasing progressively the number of data points (n) used to evaluate the linear best fit, starting with $n = 3$ and progressing until all the data in the profile had been used. For each linear fit, an error estimate was obtained:

$$\sigma(n) = \sqrt{\frac{1}{n}\sum_{i=1}^{i=n}\left(\langle u_{\mathrm{cfd}}\rangle - \langle u_{\mathrm{fit}}\rangle\right)^2}, \tag{11}$$

where $<u_{\mathrm{cfd}}>$ is the CFD prediction and $<u_{\mathrm{fit}}>$ is the velocity estimated from the linear best fit. The number of points used in the log-linear fit was then based upon seeking the local minima of σ for each velocity profile. In some cases, a local minimum was not obtained, and for these profiles, n was selected manually based on the $\sigma(n)$ profile. This was due to the vertical resolution within the log layer, resulting in nonuniform weighting effects, and as such was mainly an issue for smaller roughness lengths. For this reason, synthesis of the entire reach modeled was not practical, and so only a number of profiles distributed through the domain are investigated herein (locations defined in Figure 2). These locations were selected as they are spatially distributed across the reach and representative of the range of depths observed in the reach. Using equation (1) together with the constants (a and b) obtained from the linear regression (to the logarithmic part of the velocity profile), inferred bed shear velocity ($u^*_{\mathrm{inf}} = a\kappa$) and roughness length ($k_{s,\mathrm{inf}} = 30\exp(-b/a)$) were calculated for all values of roughness length (k_{sM}) simulated. Figures 8a and 8b show the predicted velocity profiles obtained using the fully rough log-law (equation (1)) together with the inferred roughness length and shear velocity. The results are presented for the largest and smallest roughness lengths tested.

[48] In Figure 9c, this inferred roughness length ($k_{s,\mathrm{inf}}$) is plotted as a function of the applied roughness length (k_{sM}) for all locations (P_a-P_k) indicated in Figure 2. The results for locations P_a and P_b have been highlighted by drawing a blue and black line through the respective data points. It may be expected that the inferred and applied roughness lengths should converge as denoted by the 1:1 line of agreement (Figure 9c). However, the results show that the inferred roughness length ($k_{s,\mathrm{inf}}$) is larger than the applied roughness length (k_{sM}), indicating that there needs to be an upward multiplication of k_{sM} that has parallels with that required in gravel-bed rivers [*Hey*, 1979b; *Clifford et al.*, 1992]. Natural variability in the topographic data leads to roughness effects that are transmitted to the flow through shear stresses, leading to larger energy losses than may be expected for a given roughness length. Two important points follow from this observation. First, it confirms that lower values of roughness length are required in 3-D simulations than in 2-D simulations, because roughness lengths in 3-D simulations only apply to the boundary cells, with other components of the total shear in the water column represented by explicitly modeled shear between adjacent grid cells. Importantly, this demonstrates that roughness lengths cannot be transferred simplistically between 3-D and 2-D models. Second, applying field-derived estimates of k_{sM} (obtained from extrapolation assuming a logarithmic flow profile) to a 3-D numerical simulation should be undertaken with caution and only after correction, as the estimate of k_{sM} obtained from a velocity profile ($k_{s,\mathrm{inf}}$ herein) is not equivalent to that applied to the law-of-the-wall in the near-boundary cell (k_{sM} herein). These results also show that (1) for a given location, this upscaling factor varies in a nonlinear way with increasing applied roughness length for k_{sM} less than 0.9 m and (2) for a given applied roughness length (k_{sM}), there is considerable spread in the multiplication factor that would be required to relate the inferred and applied roughness lengths depending on the location within the reach. For example, for $k_{sM} = 0.06$ m, the inferred roughness length is $k_{s,\mathrm{inf}} = 0.114$ m for location P_b and 0.0091 m for P_g.

[49] A primary reason for modeling flow in large rivers is to obtain estimates of bed shear stress. In depth-averaged simulations, the boundary shear stress is commonly estimated from the quadratic law with roughness effects estimated using the CWE (equation (2)), which assumes that the flow is log-linear over the entire flow depth. However, the model predictions (Figures 9a and 9b) show that this velocity assumption is not valid over the entire flow depth. For a given inferred roughness length ($k_{s,\mathrm{inf}}$), convergence in bed shear stress estimates between depth-averaged simulations (using the CWE) and 3-D simulations (using equation (1)) will result in divergence between the predicted depth-averaged velocity. This is a consequence of the non log-linear velocity profiles observed, most notably for smaller roughness lengths and in deeper areas of the reach. In Figures 8a and 8b, we have supplemented the 3-D model velocity profiles (for location Pa and Pb) with reconstructed velocity profiles obtained using the fully rough log-law (equation (1)). These profiles were computed assuming fully log-linear flow with the inferred roughness length ($k_{s,\mathrm{inf}}$) and shear velocity (u^*_{inf}). These represent the CWE in the case where $k_{s,\mathrm{inf}}$ is used and there is convergence in the predicted bed shear stresses.

[50] These differences are due to divergence from log-linear velocity profiles. In our simulations, the flow is log-linear over the lower part of the flow and relatively uniform close to the water surface. To account for this when applying the CWE, the roughness length applied could be upscaled to reflect the fact that only part of the flow is log-linear. Analysis of the selected velocity profiles (see Figure 2 for locations) using the solutions for the optimal roughness lengths, $k_s = 0.03$–0.06 m, show that the flow is log-linear for at least 74% of the flow depth for all but one location (P_c). For this profile, the log-linear depth was assessed to be 55% of the flow depth. This result does not point toward a simple scaling relationship and further work, which is beyond the scope of this paper, is needed to develop this further. Herein, we have concentrated on divergence from logarithmic velocity profiles and note that these functions also need to account for energy losses induced by inertia, secondary flows, and turbulence [see *Blanckaert*, 2010].

[51] *van Rijn* [1984, 2007] proposed roughness predictors based on estimates of characteristic bedforms and related these to the flow hydraulics. These predictors use depth-averaged values of the flow to predict sand roughness that can then be applied using the CWE. In 3-D flow calculations, departure from a fully logarithmic velocity profile implies divergence in bed shear estimates compared with depth-averaged simulations using the CWE. This method therefore needs to account for these differences and thus is not suitable for our 3-D simulation. However, herein we evaluate the *van Rijn* [2007] roughness predictor using the results from our 3-D CFD simulation to compare with the roughness values applied. The *van Rijn* [2007] roughness predictor is a function that returns the equivalent sand roughness ($k_{s,\mathrm{VR}}$). It is dependent on the median grain size (D_{50}), relative grain density ρ_s/ρ_w, flow depth, and depth-averaged velocity. Field measurements in the study reach suggest that $D_{50} = 350$ μm and $s = 2.02$ and values of $k_{s,\mathrm{VR}}$ were calculated for the locations identified in Figure 2 (P_a-P_k). These values were then used together with the measured depth and depth-integrated velocity predictions to compute the results presented in Figure 9d. The computed van Rijn roughness values ($k_{s,\mathrm{VR}}$) are then presented as a function of the roughness length applied in the model (k_{sM}). The results show that the equivalent roughness length ($k_{s,\mathrm{VR}}$) is largely insensitive to the value of k_{sM} applied in the model. For roughness values less than approximately 0.004 m, the *van Rijn* [2007] estimation is larger than the roughness length applied in the CFD model. For larger simulated roughness lengths (k_{sM}), the *van Rijn* [2007] estimation is significantly smaller than the applied roughness length. However, the predicted roughness lengths ($k_{s,\mathrm{VR}} = 0.12$–0.42 m) are a similar order of magnitude to the optimal roughness lengths ($k_{\mathrm{sM}} = 0.03$–0.06 m), suggesting *van Rijn*'s [2007] roughness predictor may perform well. These results highlight the difficulties associated with specifying spatially distributed roughness in 3-D models in situations where the roughness lengths are not known a priori.

3.4. Channel-Scale Primary and Secondary Flow

[52] It is useful to separate the primary and secondary components of flow, although this is not straightforward, and there are a number of methods that are widely used (see *Hey and Rainbird* [1996], for a full review). These methods involve rotating planar cross sections and reprojecting the velocities to obtain the secondary and primary components of flow. All but one [*Rozovskii*, 1957] of these methods apply the rotation to the entire cross section, which typically extends across the entire river. The assumption associated with this rotation is that the primary flow direction does not vary significantly across the section. The *Rozovskii* [1957] method is different in that rotation is applied to vertical velocity profiles based on the depth-averaged velocity at each location.

[53] *Lane et al.* [2000] tested some of these methods using model data to evaluate their usefulness in identifying secondary circulatory cells in confluent rivers and concluded that the *Rozovskii* [1957] method is very sensitive and likely to reveal secondary circulatory flow patterns. They also suggested that, for confluent channels, this rotation should be applied using two cross sections, one on either side of the mixing layer. In regions where the flow direction changes significantly across the channel, the primary flow direction may deviate significantly from the average. In these situations, identification of the primary and secondary flow becomes difficult.

[54] In large rivers, such quantitative determination of secondary flow is possible [e.g., *Richardson and Thorne*, 1998] but difficult [*Parsons et al.*, 2007; *Szupiany et al.*, 2009; *Sandbach et al.*, 2010], especially when the river contains a number of nested scales of curvature as well as channel and bar confluences, where it is difficult to apply quantitatively based rotation methods [*Lane et al.*, 2000; *Parsons et al.*, 2007]. Herein, we use cross streamlines based on the depth-averaged velocity field. Cross streamlines are defined in much the same way as streamlines but with the velocity field rotated by 90°. Since the flow is rotated by 90°, the resultant velocity vectors are, by definition, perpendicular to the primary flow direction. These cross streamlines help separate the primary and secondary flow directions and in 2-D, this can be written formally as

$$\mathrm{d}x/U_y = -\mathrm{d}y/U_x. \tag{12}$$

[55] The resultant patterns of cross streamlines and streamlines are used to define planar cross sections onto which the primary and secondary flows are projected. In Figure 10, the depth-averaged flow is represented using streamlines (blue) and cross streamlines (red, obtained using equation (12)) in the lee of the bar identified in Figure 2. The depth-averaged flow field was obtained using model results from the 3-D CFD simulations conducted as part of this work, where $k_{\mathrm{sM}} = 0.06$ m. These results were selected as they represent our best estimate of the flow based on the analysis of section 3.1. Also included here are contour plots of the bed topography and cross sections (green) that indicate the locations of the velocity cross sections presented in Figure 11. These cross sections were obtained by fitting a line (using linear least squares regression) through the data points obtained from the cross-streamline analysis for the labeled transects. For cross-section (c), two planar surfaces are used to represent the flow, and meet at what we refer to as the "hinge point." In this paper, we located the hinge point by selecting the position on the cross streamline that lies at the midpoint between the two converging streamlines. For this transect, the fitted line was forced to pass through hp_c to produce a smooth transition along the cross section.

[56] These cross sections show that just downstream of the confluence, the flow direction changes significantly. Cross-section (c) is made up of two lines joined together at the hinge point, hp_c, and there are still significant deviations between the cross section and cross streamline. This highlights the difficulties associated with selecting "representative" cross sections in large rivers. In fact, there is a case for perhaps increasing the number of planar surfaces used to represent these cross sections. However, we currently lack a methodology for the identification of multiple hinge points. One possible way forward would be to use cross streamlines at each location used to represent the flow, for example each grid cell. However, in this case, the result

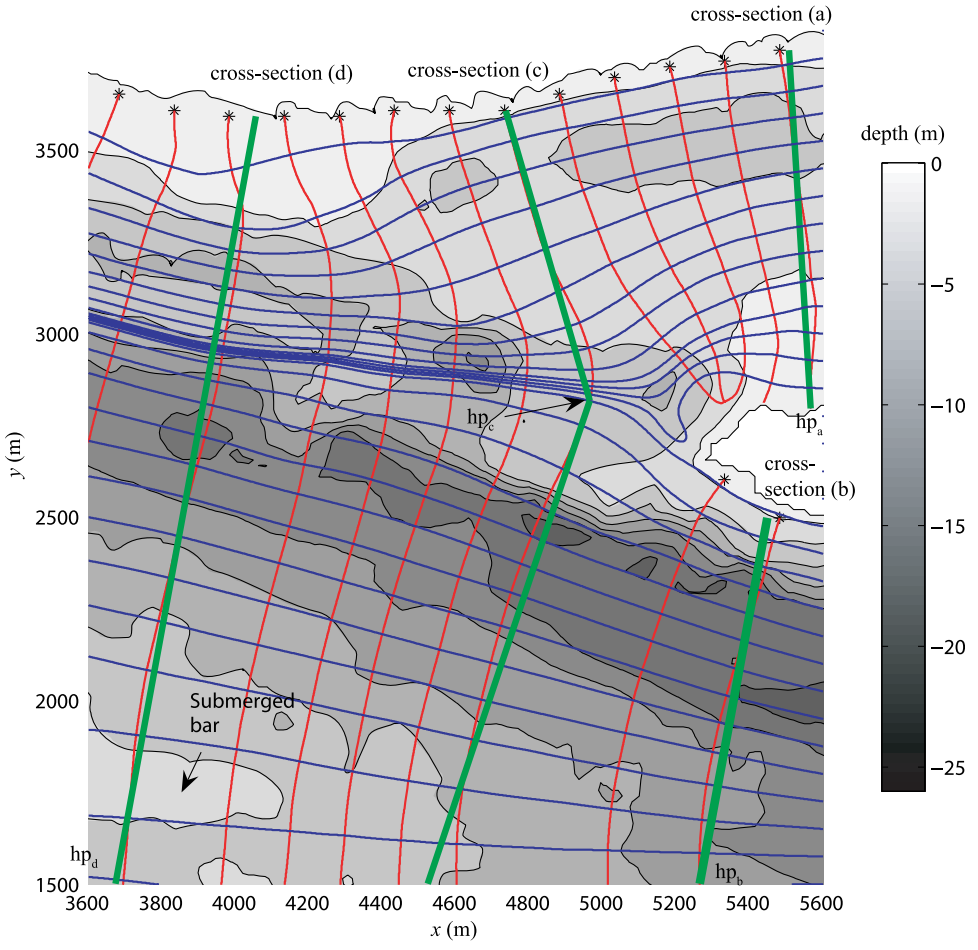

Figure 10. Representation of the flow (depth-averaged) using streamlines (blue) and cross-streamlines (red) downstream of the bar identified by the box in Figure 2. These depth-averaged values were obtained from the 3-D CFD simulations conducted as part of this work where $k_{sM} = 0.06$ m. Also included here is a contour plot of the bed topography and cross sections (green) used to rotate the data into primary and secondary flows presented in Figure 11.

is much the same as that proposed by *Rozovskii* [1957], and as such the same criticisms [*Lane et al.*, 2000] can be made.

[57] Figure 11 shows a series of plots that represent the flow in the cross sections defined in Figure 10. Here primary flow (u_p) is represented using contours, and secondary flow (u_s and u_z) is represented using vector arrows. These are presented in terms of cross-stream distance S, defined as the horizontal distance to the hinge point hp_c (see Figure 10). The cross-sectional velocities might be expected to only contain a small depth-averaged component. However, these transects are fitted to the cross streamlines using planar surfaces, and so the plane into which the primary and secondary flow are separated is not perpendicular to the depth-averaged flow vector. This results in a larger component of the depth-averaged flow projecting into the secondary flow plane and further highlights the difficulties associated with resolving primary and secondary flow in very large rivers.

[58] Cross sections (a) and (b) in Figure 11 represent the flow upstream of the confluence and show that the magnitude of the primary flow in the deeper thalweg channel (b) is larger than the shallower channel (a) to the true right of the bar. The flow in this channel also has a velocity core that is located around the center of the channel thalweg. In each of these transects (a and b), the secondary flow is principally directed towards the bar as one might expect for such a convergent situation. However, for transect (b), there is a clear divergence of flow at around $S = -400$ m, which represents around 40% of the cross section shown. This is most likely driven by upstream divergence around a submerged bar, although it may also be due partly to deviation between the transect along which the flow is projected and the cross streamline (see Figure 10) that represents the secondary flow direction. This is also a feature of transect (c), again for similar reasons.

[59] Cross-section (c) represents the flow immediately downstream of the bar and was constructed from two planar surface rotations of the velocity field. The hinge point is located at $S = 0$, which separates the flow in the shallower channel (negative S) from the deeper channel (positive S). In the shallower channel (negative S), the secondary velocities are typically small except for the region close to the hinge point (S between 0 and -400 m). This corresponds to an area where the transect deviates significantly from that of the cross streamline (see Figure 10), which influences the computed secondary flow. However, this cross section does appear to show evidence of secondary circulation. Furthermore, in a

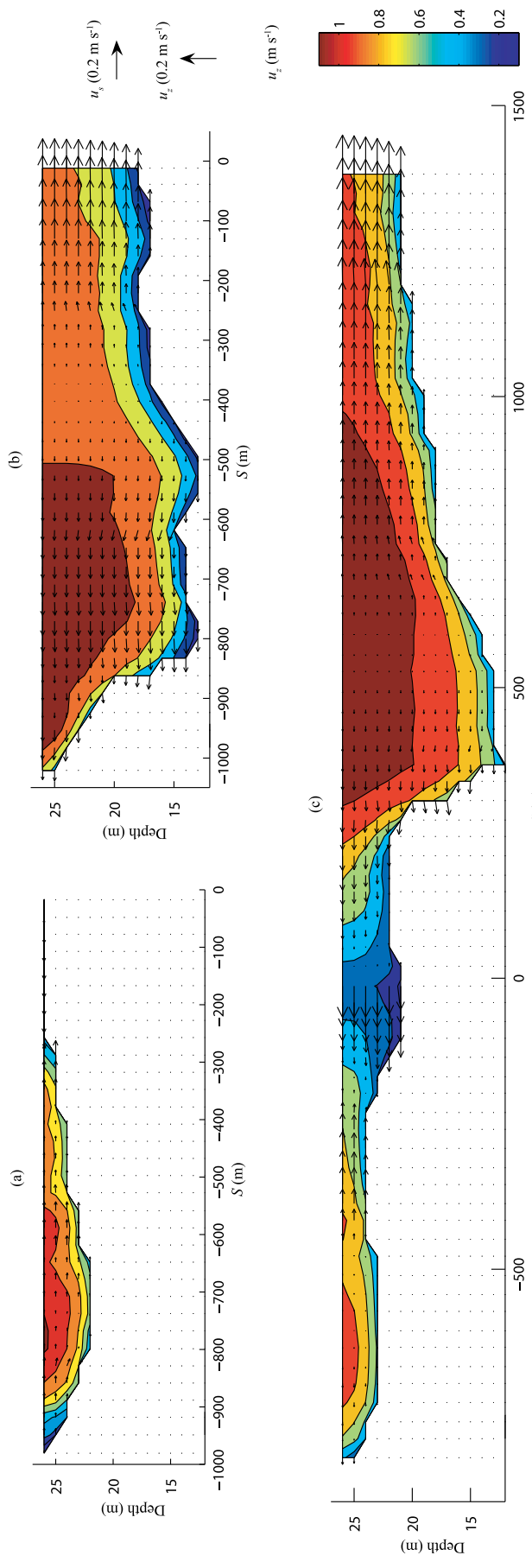

Figure 11. Cross-sectional contour plots of primary flow u_p and vector representation of secondary flow (u_s, u_z) obtained from the optimal model results ($k_{sM} = 0.06$ m). The spatial locations of these cross sections are defined in Figure 10.

similar way to transect (b), the primary flow is concentrated in the thalweg channel.

[60] Cross-section (d) represents the flow further downstream where the cross streamlines vary much less than at cross-section (c). For cross-section (d), there is no clear hinge point across the convergent streamline interface, and so a single cross section is used to represent the flow across this section of the river. The secondary flow in this cross section is largely directed toward the right bank, forced topographically by the submerged bar and the lateral shift in the channel thalweg. The primary flow in this cross section is more spread out, extending not only across part of the deeper thalweg channel but also over a shallower area of the submerged bar. This is a result of lateral migration of the channel thalweg.

[61] In summary, these results indicate that although the thalweg is the dominant topographic feature that steers flow, large-scale topography, such as bars, can also have a significant impact on the flow. The magnitude of the primary and secondary flow in the shallower channel to the true right of the bar is typically smaller than in the deeper thalweg channel. In cross-section (c), there appears to be a region of secondary circulation. However, this cross streamline deviates significantly from that of the cross section, which may significantly influence the computed secondary flow (see Figure 10). In general, these results show that there is an absence of computed secondary circulatory flow, an observation which is perhaps surprising given the convergent nature of the flow. *Parsons et al.* [2007] also observed a lack of secondary flow in a large confluence-diffluence unit approximately 40 km downstream of our study reach. *Parsons et al.* [2007] concluded that: the higher width-depth ratio associated with large rivers and the much slower adjustment of dune morphology to changes in river discharge, both may dampen secondary circulation formation. It should also be stressed, however, that the turbulence closure applied herein is isotropic and thus anisotropic turbulence-driven secondary circulation is not modeled. However, as suggested in section 2.4, laboratory and field data show that turbulence-driven secondary circulations are typically small. This absence of secondary circulation and the semi-2-D nature of the flow suggest that, in one sense, large rivers are simpler than smaller rivers and that a 2-D approach may be sufficient, enabling larger spatial and temporal scales to be investigated.

4. Discussion and Conclusions

[62] In this paper, results have been presented from a combined field and numerical modeling study of one of the world's largest sand-bed rivers, the Río Paraná, to investigate the possibility of applying CFD schemes to understand flow in very large rivers at large scales ($\sim$10 km). A series of CFD simulations were run using a range of roughness lengths to parameterize bedform effects not present in the model. The CFD model was calibrated using measured flow data and the resulting flow field investigated and interpreted.

[63] Calibration for roughness effects in numerical models is typically achieved using the reach-averaged water surface slope. However, in the Río Paraná, the water surface slope is small and difficult to measure. Optimization was therefore conducted using 3-D ADCP measurements. This data was analyzed using a number of metrics including: bias (obtained using the gradient of the regressed line), scatter (from the correlation coefficient r), and variance of the data about the 1:1 line of equality. The analysis suggests that the metrics of bias and scatter provide the most sensitive and best means of optimizing the model. The variance metric was least sensitive to changes in roughness and resulted in very different optimum roughness lengths to the bias and scatter metrics. Furthermore, analysis of the water surface slope results adds more validity to the bias and scatter metrics.

[64] Based on this analysis, our results indicate that the optimum roughness length is around $k_{sM} = 0.06$ m for this reach at the studied discharge ($\sim$15,100 m^3 s^{-1}). This is a similar order of magnitude to the intermediate roughness estimate ($k_s = 0.04$ m), which is based on reach-averaged properties such as water surface slope and flow velocity (see section 2.3). The estimate based on measured bedforms suggested roughness lengths around 0.73 m, an order of magnitude larger than the optimum. These result represent the flow at 15,100 m^3 s^{-1} which is a larger than the average ($\sim$12,000 m^3 s^{-1}) discharge for this part of the Río Paraná. They are therefore only applicable to this discharge and a fully developed understanding of flow in large rivers can only be obtained from further investigation over a range of flow conditions. This would require a number of repeat flow and topography surveys and be a significant field undertaking. Furthermore, our results show the limits of using existing wall functions for the representation of roughness effects in large rivers. Taken together, these conclusions points toward the need to develop process-based roughness closures that are centered upon the distinction between what is contained explicitly as topographic information in the model (a function of both model resolution and available topographic data) and what then has to be parameterized as roughness. As both 2-D and 3-D models represent roughness as a wall treatment, and this wall treatment is grounded in the form of the turbulence model used, the starting point has to be turbulence models that can capture the length scales associated with larger rivers.

[65] Spatial patterns of flow around, and in, the lee of a large bar were presented using the optimum CFD results. Cross-sectional velocity profiles of primary velocity magnitude and secondary velocity vectors were presented. The primary and secondary flows were resolved using a novel technique developed herein. The flow patterns indicate that although the thalweg is dominant in steering the flow, large topography, such as bars, also have a significant impact on the flow. In general, the model results show that there is an absence of secondary circulations, an observation also made by *Parsons et al.* [2007] for flow around a bar approximately 40 km downstream of this reach. The results also highlight the difficulty associated with resolving primary and secondary flows.

[66] Our results indicate that the flow is log-linear over a large portion of the flow depth, and that the flow is largely uniform above this. The depth of the log-linear layer increases for larger roughness lengths, and in the shallower areas of the flow a larger part of the flow depth is log-linear. The results also indicate that solutions obtained using the CWE (equation (2)) without correction will diverge from the results obtained using 3-D models. This correction could be incorporated through the submerged roughness, h/k_s, achieved

by upscaling the applied roughness length k_s. However, our results did not provide evidence for a simple scaling relationship. The semi-2-D nature of the flow and the absence of secondary circulation suggest that large rivers may be investigated using simpler 2-D approaches. This simplification opens up the possibility that much larger spatial- and temporal-scales can therefore be investigated. The present model results also show that changing roughness lengths results in the deeper channels routing more of the flow, and that this was especially sensitive for smaller roughness lengths.

[67] These velocity profiles were further analyzed using linear regression in log-linear space to obtain estimates of roughness lengths (inferred roughness). The results show that these estimates ($k_{s,\mathrm{inf}}$) are larger than the applied roughness length (k_{sM}), which is perhaps counterintuitive, as they may expected to be equal. However, topographic variability produces roughness effects that are transmitted to the flow, thereby leading to larger inferred roughness lengths than applied. This additional effect must therefore be included when inferring roughness from field-derived estimates. We also computed roughness lengths using *van Rijn*'s [2007] roughness estimator and flow velocities from these extracted profiles. The computed roughness lengths were largely insensitive to changes in modeled roughness length. For the selected velocity profiles, the predicted roughness lengths ($k_{s,\mathrm{VR}} = 0.12$–0.42 m) were a similar order of magnitude to the optimal roughness lengths ($k_{\mathrm{sM}} = 0.03$–0.06 m), suggesting *van Rijn*'s [2007] roughness predictor may perform well. However, these estimates are based on depth-integrated results and so there is a need to rescale these results.

[68] Future work should aim to assess whether or not empirical or semiphysical generalizations can be developed that model the additional parameters needed to upscale roughness lengths appropriately in 3-D CFD simulations. This must also address any "morphodynamic lag" that may lead to damping of secondary circulation [*Parsons et al.*, 2007]. If such generalizations cannot be developed, then roughness representation may be better focused upon explicit measurement and representation of bedforms in much higher-resolution CFD applications than in development of effective roughness parameterizations. As already discussed, this limits the spatial scale that can be modeled and may only be representative of a small range of flow conditions. Furthermore, until such relationships are developed, applications of both 2-D and 3-D CFD models need to explore roughness-length sensitivity as part of a wider analysis of model uncertainty.

[69] **Acknowledgments.** The authors are grateful to the UK Natural Environment Research Council (NERC) for their financial support (grant number NE/E016022/1) and the staff of CECOAL CONICET (Corrientes, Argentina) for their essential field support, in particular the help and skills of Lolo Roberto. The authors also thank Chris Simpson for producing the final figures, Koen Blanckaert, and two anonymous referees who produced especially helpful reviews that have helped shape this paper.

References

Abad, J. D., B. L. Rhoads, I. Guneralp, and M. H. Garcia (2008), Flow structure at different stages in a meander-bend with bendway weirs, *J. Hydraul. Eng.*, *134*(8), 1052–1063, doi:10.1061/(ASCE)0733-9429(2008)134:8(1052).

Amsler, M. L., and M. H. Garcia (1997), Sand-dune geometry of large rivers during floods—Discussion, *J. Hydraul. Eng.*, *123*(6), 582–585, doi:10.1061/(ASCE)0733-9429(1997)123:6(582).

Ashworth, P. J., and R. I. Ferguson (1986), Interrelationships of channel processes, changes and sediment in a proglacial braided river, *Geograf. Annal. Ser. A Geogr.*, *68*(4), 361–371, doi:10.2307/521527.

Ashworth, P. J., and J. Lewin (2012), How do big rivers come to be different?, *Earth Sci. Rev.*, *114*, 84–107, doi:10.1016/j.earscirev.2012.05.003.

Ashworth, P. J., R. I. Ferguson, P. E. Ashmore, C. Paola, D. M. Powell, and K. L. Prestegaard (1992), Measurements in a braided river chute and lobe: 2. Sorting of bed-load during entrainment, transport, and deposition, *Water Resour. Res.*, *28*(7), 1887–1896, doi:10.1029/92WR00702.

Ashworth, P. J., J. L. Best, J. Roden, C. S. Bristow, and G. J. Klaassen (2000), Morphological evolution and dynamics of a large, sand braid-bar, Jamuna River, Bangladesh, *Sedimentology*, *47*, 533–555, doi:10.1046/j.1365-3091.2000.00305.x.

Biron, P. M., S. N. Lane, A. G. Roy, K. F. Bradbrook, and K. S. Richards (1998), Sensitivity of bed shear stress estimated from vertical velocity profiles: The problem of sampling resolution, *Earth Surf. Process. Landforms*, *23*(2), 133–139, doi:10.1002/(SICI)1096-9837(199802)23:2133::AID-ESP824>3.0.CO;2-N.

Blanckaert, K. (2009), Saturation of curvature induced secondary flow, energy losses and turbulence in sharp open-channel bends. Laboratory experiments, analysis and modelling, *J. Geophys. Res.*, *114*, F03015, doi:10.1029/2008JF001137.

Blanckaert, K. (2010), Topographic steering, flow recirculation, velocity redistribution and bed topography in sharp meander bends, *Water Resour. Res.*, *46*, W09506, doi:10.1029/2009WR008303.

Blanckaert, K., and H. J. de Vriend (2003), Non-linear modeling of mean flow redistribution in curved open channels, *Water Resour. Res.*, *39*(12), 1375, doi:10.1029/2003WR002068.

Blanckaert, K., and H. J. de Vriend (2010), Meander dynamics: A 1D flow model without curvature restrictions, *J. Geophys. Res.*, *115*, F04011, doi:10.1029/2009JF001301.

Booker, D. J. (2003), Hydraulic modelling of fish habitat in urban rivers during high flows, *Hydrol. Process.*, *17*, 577–599, doi:10.1002/hyp.1138.

Booker, D. J., D. A. Sear, and A. J. Payne (2001), Modelling three-dimensional flow structures and patterns of boundary shear stress in a natural pool-riffle sequence, *Earth Surf. Process. Landforms*, *26*(5), 553–576, doi:10.1002/esp.210.

Booker, D. J., M. J. Dunbar, and A. Ibbotson (2004), Predicting juvenile salmonid drift-feeding habitat quality using a three-dimensional hydraulic-bioenergetic model, *Ecol. Modell.*, *177*(1–2), 157–177, doi:10.1016/j.ecolmodel.2004.02.006.

Bradbrook, K. F., S. N. Lane, and K. S. Richards (2000), Numerical simulation of time-averaged flow structure at river channel confluences, *Water Resour. Res.*, *36*, 2731–2746, doi:10.1029/2000WR900011.

Carney, S. K., B. P. Bledsoe, and D. Gessler (2006), Representing the bed roughness of coarse-grained streams in computational fluid dynamics, *Earth Surf. Process. Landforms*, *31*(6), 736–746, doi:10.1002/esp.1274.

Casas, M. A., S. N. Lane, R. J. Hardy, G. Benito, and P. J. Whiting (2010), Reconstruction of subgrid scale topographic variability and its effect upon the spatial structure of three dimensional river flow, *Water Resour. Res.*, *46*, W03519, doi:10.1029/2009WR007756.

Clifford, N. J., A. Robert, and K. S. Richards (1992), Estimation of flow resistance in gravel-bedded rivers—A physical explanation of the multiplier of roughness length, *Earth Surf. Process. Landforms*, *17*(2), 111–126, doi:10.1002/esp.3290170202.

Constantinescu, G., M. Koken, and J. Zeng (2011), The structure of turbulent flow in an open channel bend of strong curvature with deformed bed: insight provided by detached eddy simulation, *Water Resour. Res.*, *47*, W05515, doi:10.1029/2010WR010114.

Colebrook, C. F., and M. White (1937), The reduction of carrying capacity of pipes with age, *J. Inst. Civil Eng.*, *7*(1), 99–118, doi:10.1680/ijoti.1937.14682.

Dargahi, B. (2004), Three-dimensional flow modelling and sediment transport in the River Klaralven, *Earth Surf. Process. Landforms*, *29*, 821–852, doi:10.1002/esp.1071.

Drago, E. C., and M. L. Amsler (1998), Bed sediment characteristics in the Paraná and Paraguay rivers, *Water Int.*, *23*, 174–183, doi:10.1080/02508069808686764.

Einstein, H., and H. Li (1958), Secondary currents in straight channels, *Trans. Am. Geophys. Union*, *39*, 1085–1088.

Ercan, A., and B. A. Younis (2009), Uncertainties in the prediction of flow in a long reach of the Sacramento River, *Water Environ. J.*, *23*(4), 272–285, doi:10.1111/j.1747-6593.2008.00113.x.

Escauriaza, C., and F. Sotiropoulos (2011), Initial stages of erosion and bed form development in a turbulent flow around a cylindrical pier, *J. Geophys. Res.*, *116*, F03007, doi:10.1029/2010JF001749.

Ferguson, R. I. (2007), Flow resistance equations for gravel- and boulder-bed streams, *Water Resour. Res.*, *43*, W05427, doi:10.1029/2006WR005422.

Ferguson, R. I., D. R. Parsons, S. N. Lane, and R. J. Hardy (2003), Flow in meander bends with recirculation at the inner bank, *Water Resour. Res.* *39*(11), 1322, doi:10.1029/2003WR001965.

Garcia, M. H. (2006), Sediment transport and morphodynamics, in *Sedimentation Engineering: Processes, Measurements, Modeling, and Practice, ASCE Manuals and Reports on Engineering Practice*, no. 110, edited by M. H. Garcia, pp. 26–146, Reston, Va., doi:10.1061/40856(200)94.

Gupta, A. (2007), *Large Rivers: Geomorphology and Management*, Wiley, Chichester, U. K.

Haff, P. K. (1996), Limitations on predictive modelling in geomorphology, in *The Scientific Nature of Geomorphology*, edited by B. L. Rhoads and C. E. Thorn, pp. 337–358, Wiley, Chichester, U. K.

Hardy, R. J., S. N. Lane, R. I. Ferguson, and D. R. Parsons (2003), Assessing the credibility of a series of computational fluid dynamic simulations of open channel flow, *Hydrol. Process.*, *17*(8), 1539–1560, doi:10.1002/hyp.1198.

Hardy, R. J., S. N. Lane, M. R. Lawless, J. L. Best, L. Elliot, and D. B. Ingham (2005), Development and testing of numerical code for treatment of complex river channel topography in three-dimensional CFD models with structured grids, *J. Hydraul. Res.*, *43*(5), 468–480, doi:10.1080/00221680509500145.

Hardy, R. J., D. R. Parsons, J. L. Best, S. N. Lane, R. Kostaschuck, and O. Orfeo (2006), Three-dimensional modelling of flows over a natural dune field, in *River Flow 2006*, edited by R. M. L. Ferreria et al., pp. 1077–1083, Taylor and Francis, London.

Hey, R. D. (1979a), Flow resistance in gravel-bed rivers, *J. Hydraul. Div.*, *105*(4), 365–379.

Hey, R. D. (1979b), Dynamic process-response model of river channel development, *Earth Surf. Process. Landforms*, *4*, 59–72, doi:10.1002/esp.3290040106.

Hey, R. D., and P. C. B. Rainbird (1996), Three dimensional in straight and curved reaches, in *Advances in Fluvial Dynamics and Stratigraphy*, edited by P. A. Carling and M. R. Dawson, pp. 33–66, Wiley, Chichester, U. K.

Hodskinson, A. (1996), Computational fluid dynamics as a tool for investigating separated flow in river bends, *Earth Surf. Process. Landforms*, *21*(11), 993–1000, doi:10.1002/(SICI)1096-9837(199611)21:11<993::AID-ESP698>3.0.CO;2-R.

Hodskinson, A., and R. I. Ferguson (1998), Numerical modelling of separated flow in river bends: Model testing and experimental investigation of geometric controls on the extent of flow separation at the concave bank, *Hydrol. Process.*, *12*(8), 1323–1338, doi:10.1002/(SICI)1099-1085(19980630)12:8<1323::AID-HYP617>3.0.CO;2-S.

Ingham, D. B., and L. Ma (2005), Fundamental equations for CFD in river flow simulations, in *Computational Fluid Dynamics: Applications in Environmental Hydraulics*, edited by P. D. Bates et al., pp. 19–54, Wiley, Chichester, U. K.

Kamphuis, J. W. (1974) Determination of sand roughness for fixed beds, *J. Hydraul. Res.*, *12*(2), 193–203,doi:10.1080/00221687409499737.

Kang, S., and F. Sotiropoulos (2011), Flow phenomena and mechanisms in a field scale experimental meandering stream with a pool-riffle sequence: Insight gained via numerical simulation, *J. Geophys. Res.*, *116*, F03011, doi:10.1029/2010JF001814.

Kleinhans, M. G., H. R. A. Jagers, E. Mosselman, and C. J. Sloff (2008), Bifurcation dynamics and avulsion duration in meandering rivers by one-dimensional and three-dimensional models, *Water Resour. Res.*, *44*, W08454, doi:10.1029/2007WR005912.

Kostaschuk, R., P. V. Villard, and J. L. Best (2004), Measuring velocity and shear stress over dunes with acoustic Doppler profiler, *J. Hydraul. Eng.*, *6130*(9), 932–936, doi:10.1061/(ASCE)0733-9429(2004)130:9(932).

Kostaschuk, R., J. L. Best, P. V. Villard, J. Peakall, and M. Franklin (2005), Measuring flow velocity and sediment transport with an acoustic Doppler current profiler, *Geomorphology*, *68*, 25–37, doi:10.1016/j.geomorph.2004.07.012.

Kostaschuk, R., D. Shugar, J. L. Best, D. R. Parsons, S. N. Lane, R. J. Hardy, and O. Orfeo (2009), Suspended sediment transport and deposition over a dune: Rio Paraná, Argentina. *Earth Surf. Process. Landforms*, *34*(12), 1605–1611, doi:10.1002/esp.1847.

Lane, S. N. (2005), Roughness—Time for a re-evaluation?, *Earth Surf. Process. Landforms*, *30*(2), 251–253, doi:10.1002/esp.1208.

Lane, S. N., and K. S. Richards (1998), Two-dimensional modelling of flow processes in a multi-thread channel, *Hydrol. Process.*, *12*(8), 1279–1298, doi:10.1002/(SICI)1099-1085(19980630)12:8<1279::AID-HYP615>3.0.CO;2-E.

Lane, S. N., J. H. Chandler, and K. S. Richards (1994), Developments in monitoring and terrain modelling small-scale river-bed topography, *Earth Surf. Process. Landforms*, *19*(4), 349–368, doi:10.1002/esp.3290190406.

Lane, S. N., K. F. Bradbrook, K. S. Richards, P. A. Biron, and A. G. Roy (1999), The application of computational fluid dynamics to natural river channels: Three-dimensional versus two-dimensional approaches, *Geomorphology*, *29*(1–2), 1–20, doi:10.1016/S0169-555X(99)00003-3.

Lane, S. N., K. F. Bradbrook, K. S. Richards, P. M. Biron, and A. G. Roy (2000), Secondary circulation cells in river channel confluences: measurement artefacts or coherent flow structures?, *Hydrol. Process.*, *14*(11–12), 2047–2071, doi:10.1002/1099-1085(20000815/30)14:11/12<2047::AID-HYP54>3.0.CO;2-4.

Lane, S. N., R. J. Hardy, L. Elliot, and D. B. Ingham (2004), Numerical modeling of flow processes over gravelly surfaces using structured grids and a numerical porosity treatment, *Water Resour. Res.*, *40*(1), W01302, doi:10.1029/2002WR001934.

Lane, S. N., D. R. Parsons, J. L. Best, O. Orfeo, R. Kostaschuk, and R. J. Hardy (2008), Causes of rapid mixing at a junction of two large rivers: Río Paraná and Río Paraguay, Argentina, *J. Geophys. Res.*, *113*(F2), F02024, doi:10.1029/2006JF000745.

Latrubesse, E. M. (2008), Patterns of anabranching channels: The ultimate end-member adjustment of mega rivers, *Geomorphology*, *101*(1–2), 130–145, doi:10.1016/j.geomorph.2008.05.035.

Launder, B. E., and W. Ying (1973), Prediction of flow and heat transfer in ducts of square cross-section, *Proc. Inst. Mech. Eng.*, *187*, 455–461.

Launder B. E., G. J. Reece, and W. Rodi (1975), Progress in the development of a Reynolds stress turbulence closure, *J. Fluid Mech.*, *68*, 537–566, 1975, doi:10.1017/S0022112075001814.

Lien, F. S., and M. A. Leschziner (1994a) Assessment of turbulence-transport models including non-linear rng eddy-viscosity formulation and second-moment closure for flow over a backward-facing step, *Comput. Fluids*, *23*(8), 983–1004, doi:10.1016/0045-7930(94)90001-9.

Lien, F. S., and M. A. Leschziner (1994b), Upstream monotonic interpolation for scalar transport with application to complex turbulent flows, *Int. J. Numer. Methods Fluids*, *19*, 527–548, doi:10.1002/fld.1650190606.

Ma, L., P. J. Ashworth, J. L. Best, L. Elliot, D. B. Ingham, and L. J. Whitcombe (2002), Computational fluid dynamics and the physical modelling of an upland urban river, *Geomorphology*, *44*(3–4), 375–391, doi:10.1016/S0169-555X(01)00184-2.

Mahmood, K. (1971), Flow in sand bed channels, *Water Management Technical Rep. 11*, Colorado State Univ., Fort Collins, Colo.

Martinelli, L., and V. Yakhot (1989), RNG-based turbulence approximations with application to transonic flows, paper presented at 9th Computational Fluid Dynamics Conference, Buffalo, New York, AIAA-89-1950, American Institute of Aeronautics and Astronautics, Reston, Va.

McLelland, S. J., P. J. Ashworth, J. L. Best, J. Roden, and G. J. Klaassen (1999), Flow structure and spatial distribution of suspended sediment around an evolving braid bar, Jamuna River, Bangladesh, in *Fluvial Sedimentology VI, Spec. Publ. Int. Assoc. Sedimentol.*, edited by N. D. Smith, pp. 43–57, Blackwell, Oxford.

Morvan, H., G. Pender, N. G. Wright, and D. A. Ervine (2002), Three-dimensional hydrodynamics of meandering compound channels, *J. Hydraul. Eng.*, *128*, 674–682, doi:10.1061/(ASCE)0733-9429(2002)128:7(674).

Nabi, M. A. (2008a), Three-dimensional model of detailed hydrodynamics for simulation of subaqueous dunes, in *Marine and River Dune Dynamics III*, edited by D. R. Parsons et al., pp. 235–240, Leeds, U. K.

Nabi, M. A. (2008b), A 3D model of detailed hydrodynamics with sediment transport for simulation of subaqueous dunes, in *River Flow 2008*, edited by M. Altinakar et al., pp. 1423–1431, Kubaba Congress Dept. and Travel Services, Cesme-Izmir, Turkey.

Nezu, I., and W. Rodi (1985), Experimental study on secondary currents in open channel flow, in *Proc. 21st Congress of the IAHR*, Melbourne, Australia, 2, 115–119.

Nicholas, A. P. (2001), Computational fluid dynamics modelling of boundary roughness in gravel-bed rivers: An investigation of the effects of random variability in bed elevation, *Earth Surf. Process Landforms*, *26*(4), 345–362, doi:10.1002/esp.178.

Nicholas, A. P. (2005), Roughness parameterization in CFD modeling of gravel-bed rivers, in *Computational Fluid Dynamics: Applications in Environmental Hydraulics*, edited by P. D. Bates et al., pp. 329–355, Wiley, Chichester, U. K.

Nicholas, A. P., et al. (2012), Modelling hydrodynamics in the Rio Paraná, Argentina: an evaluation and inter-comparison of reduced-complexity and physics-based models applied to a large sand-bed river, *Geomorphology*, *169–170*, 192–211, doi:10.1016/j.geomorph.2012.05.014.

Nikora, V., I. McEwan, S. McLean, S. Coleman, D. Pokrajac, and R. Walters (2007a), Double-averaging concept for rough-bed open-channel and overland flows: Theoretical background, *J. Hydraul. Eng.*, *133*(8), 873–883, doi:10.1061/(ASCE)0733-9429(2007)133:8(873).

Nikora, V., S. McLean, S. Coleman, D. Pokrajac, I. McEwan, L. Campbell, J. Aberle, D. Clunie, and K. Koll. (2007b), Double-averaging concept for rough-bed open channel and overland flows: Applications, *J. Hydraul. Eng.*, *133*(8), 884–895, doi:10.1061/(ASCE)0733-9429(2007)133:8(884).

Nikuradse, J. (1933), Laws for flows in rough pipes, translated from German [Stromungsgesetz in rauhren Rohen], *NACA Tech. Memo. 1292*, 62 pp., Natl. Advisory Commission for Aeronautics, Washington, D. C.

Oberg, K., and D. S. Mueller (2007), Validation of streamflow measurements made with acoustic Doppler current profilers, *J. Hydraul. Eng.*, *133*(12), 1421–1432, doi:10.1061/(ASCE)0733-9429(2007)133:12(1421).

Olsen, N. R. B. (2003), Three-dimensional CFD modeling of self-forming meandering channel, *J. Hydraul. Eng.*, *129*, 366–372, doi:10.1061/(ASCE)0733-9429(2003)129:5(366).

Olsen, N. R. B., and S. Stokseth (1995), Three-dimensional numerical modelling of water flow in a river with large bed roughness, *J. Hydraul. Res.*, *33*(4), 571–581, doi:10.1080/00221689509498662.

Onitsuka K., and I. Nezu (2001), Numerical prediction of rectangular open channel flow by using large eddy simulation, in *Proceedings of the 29th Congress of IAHR*, Beijing, China, International Association for Hydro-Environment Engineering and Research, pp. 196–203.

Orfeo, O., and J. Stevaux (2002), Hydraulic and morphologic characteristics of middle and upper reaches of the Paraná River (Argentina and Brazil), *Geomorphology*, *44*(3/4), 309–322, doi:10.1016/S0169-555X(01)00180-5.

Paarlberg, A. J., C. M. Dohmen-Janssen, S. J. M. H. Hulscher, P. Termes, and R. Schielen (2010), Modelling the effect of time-dependent river dune evolution on bed roughness and stage, *Earth Surf. Process. Landforms*, *35*, 1854–1866, doi:10.1002/esp.2074.

Parsons, D. R., J. L. Best, O. Orfeo, R. J. Hardy, R. A. Kostaschuk, and S. N. Lane (2005), Morphology and flow fields of three-dimensional dunes, Río Paraná, Argentina: Results from simultaneous multibeam echo sounding and acoustic Doppler current profiling, *J. Geophys. Res.*, *110*, F04S03, doi:10.1029/2004JF000231.

Parsons, D. R., J. L. Best, S. N. Lane, O. Orfeo, R. J. Hardy, and R. Kostaschuk (2007), Form roughness and the absence of secondary flow in a large confluence-diffluence, Paraná river, Argentina. *Earth Surf. Process. Landforms*, *32*(1), 155–162, doi:10.1002/esp.1457.

Patankar, S. V., and D. B. Spalding (1972), A calculation procedure for heat, mass and momentum transfer in three-dimensional parabolic flows, *Int. J. Heat Mass Transfer*, *15*(10), 1787–1806. doi:10.1016/0017-9310(72)90054-3.

Potter, P. E. (1978), Significance and origin of big rivers, *J. Geol.*, *86*, 13–33.

Prandtl, L. (1926), Erste Erfahrungen mit dem rotierenden Laboratorium, *Naturwissenschaften*, *14*, 425–427.

Ramonell, C. G., Amsler, M. L., Toniolo, H. (2002), Shifting modes of the Paraná River thalweg in its middle/lower reach, *Zeitsch. Geomorphol., Suppl.*, *129*, 129–142.

Rennie, C. D., and F. Rainville (2006), Case study of precision of GPS differential correction strategies: Influence on aDcp Velocity and discharge estimates, *J. Hydraul. Eng.*, *132*(3), 225–234, doi:10.1061/(ASCE)0733-9429(2006)132:3(225).

Rennie, C. D., G. M. Robert, and M. A. Church (2002), Measurement of bed load velocity using an acoustic Doppler current profiler, *J. Hydraul. Eng.*, *128*(5), 473–483, doi:10.1061/(ASCE)0733-9429(2002)128:5(473).

Richardson, W. R., and C. R. Thorne (1998), Secondary currents around braid bar in Brahmaputra river, Bangladesh. *J. Hydraul. Eng.*, *124*(3), 325–328, doi:10.1061/(ASCE)0733-9429(1998)124:3(325).

Rodi, W. (1993), *Turbulence Models and Their Application in Hydraulics*, 3rd ed., IAHR Monograph, Balkema, Rotterdam, Netherlands.

Rodriguez, J. F., F. A. Bombardelli, M. H. Garcia, K. M. Frothingham, B. L. Rhoads, and J. D. Abad (2004), High-resolution numerical simulation of flow through a highly sinuous river reach, *Water Resour. Manage.*, *18*(3), 177–199, doi:10.1023/B:WARM.0000043137.52125.a0.

Rozovskii, I. L. (1957), Flow of water in bends of open channels, Akad. Sci. Ukrainian SSR, Kiev, translated from Russian by Isr. Program for Sci. Transl., Jerusalem, 1961.

Ruther, N., and N. R. B. Olsen (2007), Modelling free-forming meander evolution in a laboratory channel using three-dimensional computational fluid dynamics, *Geomorphology*, *89*(3–4), 308–319, doi:10.1016/j.geomorph.2006.12.009.

Ruther, N., J. M. Singh, N. R. B. Olsen, and E. Atkinson (2005), 3-D computation of sediment transport at water intakes, *Water Manage.*, *158*, 1–7.

Sambrook Smith, G. H., P. J. Ashworth, J. L. Best, I. A. Lunt, O. Orfeo, and D. R. Parsons (2009), The sedimentology and alluvial architecture of a large braid bar, Río Paraná, Argentina, *J. Sediment. Res.*, *79*, 629–642, doi:10.2110/jsr.2009.066.

Sandbach, S. D., et al. (2010), Three-dimensional modelling of a very large river: The Río Paraná, in *River Flow 2010*, edited by A. Dittrich et al., pp. 409–417, Bundesanstalt fuer Wasserbau, Brawnschehhe, Germany.

Shen, Y., and P. Diplas (2008), Application of two- and three-dimensional computational fluid dynamics models to complex ecological stream flows, *J. Hydrol.*, *348*(1–2), 195–214, doi:10.1016/j.jhydrol.2007.09.060.

Shugar, D., R. Koastaschuk, J. L. Best, D. R. Parsons, S. N. Lane, O. Orfeo, and R. J. Hardy (2010), On the relationship between flow and suspended sediment transport over a crest of a sand dune, Río Paraná, Argentina, *Sedimentology*, *57*(1), 252–272, doi:10.1111/j.1365-3091.2009.01110.x.

Sotiropoulos, F. (2005), Introduction to statistical turbulence modelling for hydraulic engineering flows, in *Computational Fluid Dynamics: Applications in Environmental Hydraulics*, edited by P. D. Bates et al., pp. 91–120, Wiley, Chichester, U. K.

Speziale, C. G. (1987), On nonlinear K-l and K-epsilon models of turbulence, *J. Fluid Mech.*, *178*, 459–475, doi:10.1017/S0022112087001319.

Szupiany, R. N., M. L. Amsler, J. L. Best, and D. R. Parsons (2007), Comparison of fixed- and moving-vessel flow measurements with an aDp in a large river. *J. Hydraul. Eng.*, *133*(12), 1299–1309, doi:10.1061/(ASCE)0733-9429(2007)133:12(1299).

Szupiany R. N., M. L. Amsler, D. R. Parsons, and J. L. Best (2009), Morphology, flow structure, and suspended bed sediment transport at two large braid-bar confluences. *Water Resour. Res.*, *45*, W05415, doi:10.1029/2008WR007428, 2009.

Tritthart, M., and D. Gutknecht (2007), 3-D computation of flood processes in sharp river bends, *Water Manage.*, *160*, 233–247, doi:10.1680/wama.2007.160.4.233.

Tritthart, M., M. Liedermann, and H. Habersack (2009), Modelling spatio-temporal flow characteristics in groyne fields, *River Res. Applicat.*, *25*(1), 62–81, doi:10.1002/rra.1169.

van Balen W., W. S. J. Uijttewaal, and K. Blanckaert (2010), Large-eddy simulation of a curved open-channel flow over topography, *Phys. Fluids*, *22*, 075108, doi:10.1063/1.3459152.

van Rijn, L. C. (1984), Sediment transport, Part III: Bed forms and alluvial roughness, *J. Hydraul. Eng.*, *110*(12), 1733–1754, doi:10.1061/(ASCE)0733-9429(1984)110:12(1733).

van Rijn, L. C. (2007), Unified view of sediment transport by currents and waves. I: Initiation of motion, bed roughness, and bed-load transport, *J. Hydraul. Eng.*, *133*(6), 649–667, doi:10.1061/(ACSE)0733-9429(2007)133:6(649).

Versteeg, H., and W. Malalasekra (2007), *An Introduction to Computational Fluid Dynamics: The Finite Volume Method*, 2nd ed., Pearson Prentice Hall, Upper Saddle River, N. J.

Viscardi, J. M., A. Pujol, V. Weibrecht, G. H. Jirka, and N. R. Olsen (2006), Numerical simulations on the Paraná de las Palmas River, in *River Flow 2006*, edited by R. M. L. Ferreria et al., pp. 367–377, Taylor and Francis, London.

Whiting, P. J., and W. E. Dietrich (1991), Convective accelerations and boundary shear stress over a channel bar, *Water Resour. Res.*, *27*, 783–796, doi:10.1029/91WR00083.

Wiberg, P. L., and J. D. Smith (1991), Velocity distribution and bed roughness in high-gradient streams, *Water Resour. Res.*, *27*, 825–838, doi:10.1029/90WR02770.

Yakhot, V., S. A. Orszag, S. Thangam, T. B. Gatski, and C. G. Speziale (1992), Development of turbulence models for shear flows by a double expansion technique, *Phys. Fluids A*, *4*(7), 1510–1520, doi:10.1063/1.858424.

Zeng, J., G. Constantinescu, K. Blanckaert, and L. Weber (2008), Flow and bathymetry in sharp open-channel bends: Experiments and predictions, *Water Resour. Res.*, *44*, W09401, doi:10.1029/2007WR006303.